photonics

MDPI

Review

Metasurface-Enhanced Sensing Platforms for Chemical, Biological, and Environmental Monitoring: Recent Advances and Future Perspectives

Jingjing Shao [1,*], Jingyao Bian [1], Linfeng Ju [2], Tianyu Du [1], Zhiyang Zhang [1], Yanhao Kang [1], Yuhao Wang [1], Jingyue Zhang [1], Hongwei Ding [1], Feng Wang [1] and Hongliang Li [3,*]

[1] College of Science, Heilongjiang University of Science and Technology, Harbin 150022, China; bianjingyao@usth.edu.cn (J.B.); dutianyu1@usth.edu.cn (T.D.); zhangzhiyang@usth.edu.cn (Z.Z.); kangyanhao@usth.edu.cn (Y.K.); wangyuhao1@usth.edu.cn (Y.W.); zhangjingyue@usth.edu.cn (J.Z.); dinghongwei1@usth.edu.cn (H.D.); wangfeng@usth.edu.cn (F.W.)

[2] State Key Laboratory of Luminescence Science and Technology, Changchun Institute of Optics, Fine Mechanics and Physics, Chinese Academy of Sciences, Changchun 130033, China; julinfeng22@mails.ucas.ac.cn

[3] Key Laboratory of Multifunctional Nanomaterials and Smart Systems, Suzhou Institute of Nano-Tech and Nano-Bionics, Chinese Academy of Sciences, Suzhou 215123, China

* Correspondence: shaojingjing1@usth.edu.cn (J.S.); hlli2025@sinano.ac.cn (H.L.)

Abstract

The growing demand for sensitive, selective, and rapid detection of trace analytes in complex matrices is driving the development of compact optical sensing platforms. Metasurfaces can strengthen light–matter interactions through subwavelength field confinement and resonance engineering, thereby enhancing spectroscopic signals and sensitivity to analyte-induced refractive-index changes. This review examines the physical principles, material platforms, sensing mechanisms, and applications of metasurface-enhanced sensing in chemical analysis, biosensing, and environmental monitoring. Metallic, high-index dielectric, two-dimensional, and functional materials are discussed in relation to plasmonic and Mie resonances, Fano interference, and quasi-bound states in the continuum. Across these applications, optical enhancement alone does not guarantee strong analytical performance. Results depend on analyte access to the enhanced field, the selectivity of the sensing interface, and the extent of matrix interference. Further progress will require reproducible fabrication, stable operation, consistent evaluation protocols, validation with real samples, and readout systems suitable for portable use.

Keywords: metasurfaces; enhanced sensing; chemical sensing; biosensing; environmental monitoring

Check for updates

Received: 23 September 2026
Revised: 10 October 2026
Accepted: 14 October 2026
Published: 16 October 2026

Copyright: © 2026 by the authors. Licensee MDPI, Basel, Switzerland. This article is an open access article distributed under the terms and conditions of the Creative Commons Attribution (CC BY) license.

1. Introduction

Chemical analysis, biosensing, and environmental monitoring require sensitive, selective, and rapid measurements in complex samples [1–7]. Chromatography–mass spectrometry often depends on bulky instruments and sample preparation, while electrochemical sensors are susceptible to interfacial changes and matrix interference. Weak Raman scattering and infrared absorption further constrain compact spectroscopic measurements [8–12]. These limitations motivate optical platforms that strengthen light–analyte interactions while supporting reliable quantitative readout.

Surface plasmon resonance (SPR) [13,14], localized surface plasmon resonance (LSPR) [15,16], photonic crystals, and optical microcavities [17–19] concentrate electromagnetic energy near sensing interfaces. Such confinement supports surface-enhanced Raman scattering (SERS) and surface-enhanced infrared absorption (SEIRA) [20–23]. Practical performance nevertheless depends on optical loss, resonance linewidth, hotspot uniformity, and molecular selectivity, requiring coordinated control of field localization and interface chemistry.

Metasurfaces comprise ultrathin arrays of subwavelength elements whose geometry, arrangement, and material composition determine their optical response [24–26]. Plasmonic and Mie resonances, Fano interference, and quasi-bound states in the continuum (quasi-BICs) provide complementary control over field localization and linewidth. Unlike ideal bound states in the continuum (BICs), quasi-BICs retain finite radiative coupling for far-field excitation and readout [27–30].

This review focuses on engineered surfaces containing subwavelength resonant elements. Related SERS substrates, fiber-integrated plasmonic arrays, and photonic–plasmonic assemblies are included when they demonstrate transferable strategies for capture, recognition, field overlap, or readout; their architectures are identified explicitly. Direct near-field sensing is distinguished from systems in which metasurfaces act as sources, filters, or readout components. The microwave examples in Section 5.3.2 are treated as nonoptical extensions illustrating passive wireless sensing under their reported validation conditions.

Applications span gas analysis and catalytic monitoring [31,32], biomolecular and cellular assays [33,34], and environmental contaminants [35–37]. Microfluidics and two-dimensional materials provide control over transport and interfaces [38,39], while phase-change materials enable reconfiguration after fabrication [40]. These functions should be evaluated within the complete sensing workflow rather than as isolated optical features. Comparing the three application areas also helps distinguish shared design requirements from application-specific limitations.

High Q factors and low detection limits alone do not establish practical readiness. Chemical sensing requires selectivity; catalytic monitoring additionally requires unambiguous assignment of catalytic intermediates; biosensing requires control of nonspecific adsorption and validation in independent cohorts; environmental monitoring requires tolerance to changing conditions and low drift.

Earlier reviews have addressed metasurface optical sensors [41], dielectric biosensing [42], quantitative biosciences [43], and enhanced vibrational spectroscopy and photocatalysis [44]. However, these topics are often discussed separately, making it difficult to compare how optical enhancement translates into analytical performance across different sensing scenarios. Here, chemical, biological, and environmental applications are examined through a common framework linking resonator design, analyte delivery, recognition chemistry, matrix effects, and readout. Particular attention is given to the distinction between optical figures of merit and application-oriented evidence, including selectivity, reproducibility, complex-sample compatibility, and operational stability. Numerical predictions, experimental calibrations, and validation in complex samples are therefore considered separately.

This narrative review emphasizes studies published during 2021–2026, alongside foundational work, with a targeted literature update completed on 5 October 2026. Studies were selected for relevance, a clear physical or analytical contribution, and reported sample conditions, performance metrics, and validation. Experimental evidence was prioritized for analytical applicability; numerical studies illustrate emerging designs and are identified explicitly. Related platforms were included only where their transferable contribution was clear.

Figure 1 summarizes the sensing modalities and applications. Section 2 introduces mechanisms, metrics, and materials; Sections 3–5 compare chemical, biological, and environmental sensing; and Section 6 addresses integrated design, machine-learning validation, and reporting requirements.

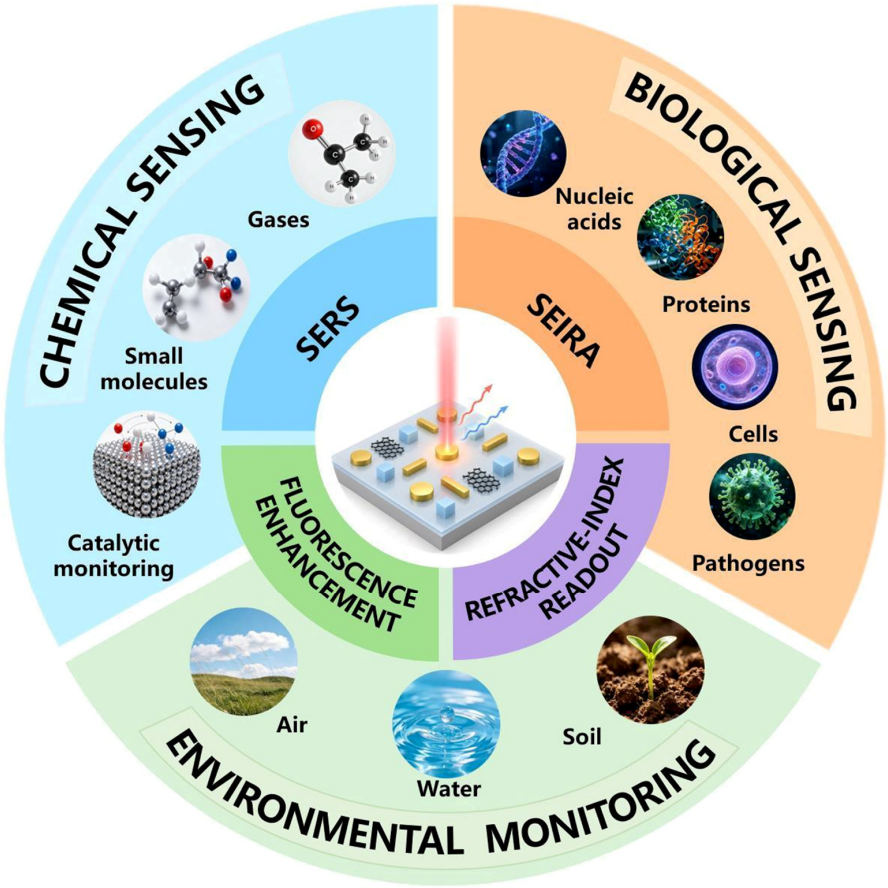


Figure 1. Overview of metasurface-enhanced sensing mechanisms and their applications in chemical, biological, and environmental monitoring.

2. Fundamental Theory and Material Systems for Metasurface-Enhanced Sensing

2.1. Basic Principles of Metasurfaces

2.1.1. Representative Resonance Modes and Their Physical Mechanisms

The resonant response of metasurfaces arises from modes supported by individual structural elements and collective coupling across the array [41,45,46]. Figure 2 summarizes representative resonances and radiation-coupling mechanisms. Fano interference and quasi-BIC behavior can occur in both plasmonic and dielectric platforms [47,48].

LSPR in metallic nanostructures arises from collective oscillations of conduction electrons driven by the incident optical field [15,49,50]. At resonance, electromagnetic fields can be strongly confined near metal surfaces, tips, and nanogaps, enhancing interactions with nearby analytes.

For an isolated metallic ellipsoid much smaller than the wavelength in a homogeneous, nonabsorbing dielectric medium, the dipolar resonance along a principal axis approximately satisfies the following condition in the quasistatic, weak-loss limit [51]:

$$\mathrm{Re}[\varepsilon_m(\omega_{\mathrm{res}})] \approx -\beta\varepsilon_d \quad (1)$$

where ω_{res} denotes the resonance angular frequency, $\varepsilon_m(\omega_{\mathrm{res}})$ is the complex relative permittivity of the metal, and ε_d is the real relative permittivity of the surrounding medium. The geometrical factor $\beta = (1 - L)/L$ is determined by the depolarization factor L along the selected principal axis. For a sphere, $L = 1/3$ and $\beta = 2$. Substrate effects, retardation, and interelement coupling require additional treatment when describing practical metasurfaces. The enhanced near fields support SERS, SEIRA, and refractive-index sensing, although ohmic losses broaden resonances and limit the Q factor [50,52,53].

High-refractive-index dielectric nanostructures support electric-dipole, magnetic-dipole, and higher-order multipolar Mie resonances [54,55]. Within spectral regions of low material absorption, nonradiative losses are small, although resonance linewidths remain dependent on radiative leakage and mode coupling. Balancing the amplitudes and phases of spectrally overlapping electric and magnetic dipole contributions can produce a Huygens response, enabling directional scattering and efficient transmission with phase control [56]. For sensing applications, the field distribution in analyte-accessible regions must also be considered to ensure sufficient spatial overlap between the resonant field and the analytes [42,57].

Fano resonances arise from coherent interference between a spectrally narrow resonant channel and a broadband background, typically producing asymmetric line shapes [47,58]. They can occur in both metallic and dielectric structures, with bright–dark mode coupling representing one common implementation. The sharp spectral features make these structures sensitive to small refractive-index changes and molecular adsorption. Their linewidth, asymmetry, and spectral contrast are governed by system dissipation and by the relative amplitudes and phases of the interfering channels [58,59].

Bound states in the continuum (BICs) are nonradiating modes whose frequencies fall within the radiation continuum but remain isolated from the available radiation channels through symmetry protection or destructive interference. For an ideal lossless structure, the radiative decay rate is zero and the corresponding quality factor formally diverges. Introducing a perturbation, such as symmetry breaking, opens a radiation channel and transforms the BIC into a radiative quasi-BIC that can be excited and measured in the far field. In fabricated devices, absorption, structural disorder, and finite array size usually reduce the attainable quality factor. A Fano line shape can arise when the quasi-BIC resonance interferes with a broadband background [48,60].

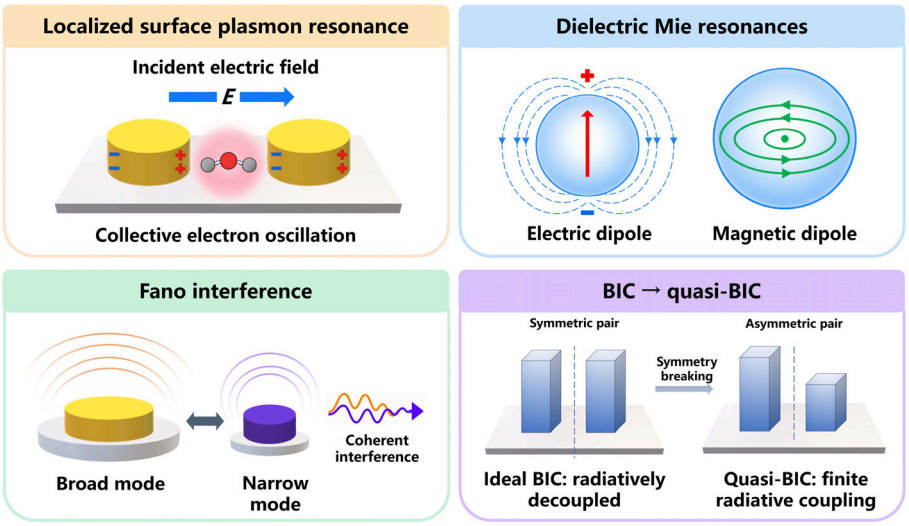


Figure 2. Representative metasurface resonances, including localized surface plasmon resonance, electric- and magnetic-dipole Mie resonances in dielectric metasurfaces, Fano interference, and BIC-to-quasi-BIC conversion through symmetry breaking.

2.1.2. Structural-Parameter Tuning and Optical-Response Design

For a fixed material platform and operating spectral range, the resonance response is governed by both the unit-cell design and the arrangement of elements within the array. Changing the size or shape of an element can shift the resonance, modify the modal field distribution, and alter the polarization response. Nanogap dimensions control the strength of near-field coupling and the location of hotspots, whereas structural and modal symmetries determine how efficiently the incident field excites a given mode [61,62].

The array period provides an additional means of controlling interelement coupling and lattice diffraction. When a localized resonance interacts with a diffractive lattice mode, a surface lattice resonance (SLR) may form. Compared with the resonance of an isolated element, an SLR can exhibit a narrower spectral linewidth [63]. This narrowing can improve the resolution of small spectral shifts, although the resulting linewidth and spectral contrast are also affected by the surrounding dielectric environment and the degree of structural order in the array [63,64].

Because these geometric parameters are often strongly interdependent, adjoint-based topology optimization and machine-learning-assisted inverse design can complement conventional parameter sweeps. Such methods are particularly useful when small changes in geometry produce coupled changes in the optical response [65–67]. For sensing applications, optimization objectives can include resonance linewidth, spectral contrast, and field overlap with analyte-accessible regions, while accounting for constraints such as minimum feature size and fabrication tolerances.

2.2. Electromagnetic-Field Enhancement and Sensing Mechanisms

Figure 3 summarizes the principal spectroscopic and refractive-index readout mechanisms discussed in this section.

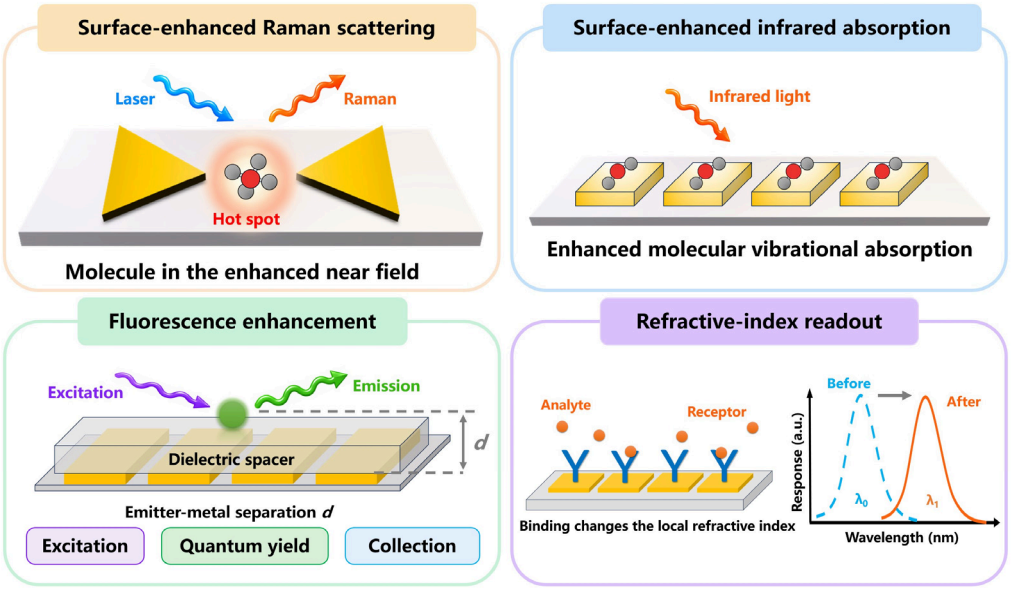


Figure 3. Schematic illustrations of four representative metasurface-enhanced sensing mechanisms: surface-enhanced Raman scattering, surface-enhanced infrared absorption, fluorescence enhancement, and refractive-index readout.

2.2.1. Local Electromagnetic-Field Enhancement

Under resonant excitation, metasurfaces can generate enhanced electromagnetic fields at structural surfaces, nanogaps, and other strongly coupled regions, thereby providing

a physical basis for detecting weak absorption and scattering signals [46,68]. Local-field enhancement can be quantified by the ratio of the squared electric-field amplitudes [69,70]:

$$G = \left| \frac{E_{loc}}{E_0} \right|^2 \quad (2)$$

where E_{loc} and E_0 denote the complex amplitudes of the local and incident electric fields, respectively. G represents the local electric-field intensity enhancement at a specified position and frequency and should not be equated with an experimentally measured spectroscopic enhancement factor.

The measured response depends on the field sampled by the analyte. Functional layers can separate bound molecules from the strongest near fields, while hotspot geometry and analyte occupancy affect the effective interaction volume. Structures with similar peak field enhancements can therefore produce different sensing responses [69,70].

2.2.2. Enhanced Light–Matter Interactions: SERS and SEIRA

SERS and SEIRA provide molecular vibrational fingerprints through Raman scattering and infrared absorption, respectively, but differ in their signal-generation mechanisms and resonance-matching requirements [68,71].

The electromagnetic contribution to SERS enhancement depends on the local-field intensity enhancements at both the excitation and Raman-scattered frequencies. When these enhancements are comparable, it can be approximated by the fourth power of the local-to-incident electric-field amplitude ratio. Chemical enhancement arising from molecule–substrate interactions should be considered separately. Characteristic Raman bands support molecular identification, whereas quantitative performance also depends on hotspot uniformity, the stability of analyte adsorption and occupancy, and batch-to-batch substrate reproducibility [68,72].

SEIRA primarily probes molecular vibrational absorption in the mid-infrared region. Effective enhancement requires spectral matching between the metasurface resonance and the target vibrational mode, together with sufficient spatial overlap between the analyte and the enhanced near field. Resonance–vibration coupling can modify the intensity and line shape of reflection or transmission spectra, allowing vibrational peak positions and spectral line shapes to support chemical identification. The measured response is also influenced by molecular orientation, resonance detuning, and background absorption. In aqueous and other complex matrices, absorption from water and coexisting matrix components must also be considered because it can interfere with the target vibrational bands [71,73,74].

2.2.3. Fluorescence Enhancement and Refractive-Index Readout

Metasurfaces can influence fluorescence excitation, decay dynamics, and signal collection by enhancing the excitation field, modifying the local density of optical states (LDOS) around emitters, and controlling emission directionality [75,76]. Under applicable single-mode and weak-coupling conditions, the Purcell effect indicates that a high Q factor and a small effective mode volume can enhance the spontaneous emission rate of an emitting dipole. The actual outcome also depends on the dipole position and orientation, spectral matching, and radiative and nonradiative losses [77].

Under weak excitation, the measured fluorescence signal is jointly determined by the excitation rate, fluorescence quantum yield, and collection efficiency. A shortened fluorescence lifetime does not necessarily indicate an increase in fluorescence intensity. For metallic structures, an excessively small molecule–metal separation can enhance nonradiative energy transfer and cause fluorescence quenching. Dielectric spacer layers or interface engineering are therefore commonly used to control the separation [78]. Molecular

specificity in fluorescence assays is primarily provided by fluorescent probes and recognition reactions, whereas metasurfaces improve excitation, emission, and signal-collection efficiencies. Au-conjugated lanthanide nanoprobes provide a related nanoparticle example of ratiometric fluorescence thermometry for monitoring photothermal heating [79].

Refractive-index readout converts analyte-induced local dielectric perturbations into changes in resonance wavelength, reflectance, or transmittance. Label-free detection can be achieved through wavelength scanning or fixed-wavelength intensity monitoring [80–82]. The magnitude of the response depends on the spatial overlap between the analytes and the resonant field, while time-resolved measurements can be used to track molecular binding, dissociation, and interfacial changes. Because refractive-index changes are not inherently molecule-specific, target recognition generally relies on functionalized interfaces. Reference channels or differential measurements can help correct for nonspecific adsorption and environmental perturbations.

2.2.4. Resonance Characteristics and Sensing Performance Metrics

Performance evaluation of resonance-based sensors should distinguish among resonance linewidth, refractive-index sensitivity, the figure of merit (FOM), and the limit of detection (LOD). The quality factor Q characterizes resonant energy confinement and is defined as 2π times the ratio of the stored energy to the energy lost per oscillation cycle. For a resonance that can be described by a single mode, Q can be expressed as

$$Q = \omega_0 / \Delta\omega \tag{3}$$

Here, ω_0 is the resonance angular frequency and $\Delta\omega$ is the linewidth associated with the resonant mode. For an approximately Lorentzian resonance, this linewidth corresponds to the spectral full width at half maximum (FWHM). For Fano resonances, however, the apparent width of an asymmetric peak or dip need not equal the modal linewidth, and a suitable Fano or coupled-mode model should be fitted to extract Q [47,48]. The measured spectrum also contains the effects of instrumental broadening, spectral sampling, illumination angle, and background subtraction. Experimental reports should therefore specify the fitting model, spectral resolution, fitting interval, and uncertainty in the extracted resonance parameters. Instrument-limited linewidths should be identified explicitly rather than interpreted as fully resolved intrinsic linewidths.

Within an approximately linear response range, the bulk refractive-index sensitivity (S) and the commonly used FOM are given by [83]:

$$S = \Delta\lambda_{res} / \Delta n \tag{4}$$

$$FOM = S / \mathrm{FWHM} \tag{5}$$

where $\Delta\lambda_{res}$ is the resonance-wavelength shift, Δn is the refractive-index change in a homogeneous surrounding medium, and FWHM is the resonance linewidth expressed in wavelength units.

A high Q factor and a large FOM can improve the resolution of small spectral shifts. However, effective detection also requires sufficient spectral contrast, spatial overlap between the analytes and the resonant mode, a high signal-to-noise ratio, and device stability [83,84]. The LOD is additionally affected by measurement noise, system resolution, baseline drift, and the calibration model and therefore cannot be inferred directly from Q or FOM. The definitions of S and FOM above primarily apply to resonance-shift refractive-index sensing. For SERS, enhancement factors and signal reproducibility should be assessed [68,72]; SEIRA requires evaluation of vibrational signal contrast and background

interference [71,73]; and fluorescence should be evaluated using intensity enhancement together with excitation conditions, quantum yield, and collection efficiency [75,78,85].

Bulk refractive-index sensitivity does not fully characterize the response to a thin surface-bound analyte layer. Under an exponential near-field model, the surface sensitivity can be related to the bulk refractive-index sensitivity by accounting for the finite thickness of the surface layer [86]:

$$S_S = S_B(1 - e^{-\frac{2t}{L_d}}) \tag{6}$$

where S_S is the refractive-index sensitivity of a uniform surface layer at a fixed thickness t, and S_B is the bulk refractive-index sensitivity; both are expressed in nanometers per refractive-index unit (nm/RIU) when wavelength shifts are measured in nanometers. L_d denotes the decay length of the electric-field amplitude, so the corresponding intensity decay gives the factor of 2 in the exponent. This approximation assumes a weakly perturbing layer directly adjacent to the sensing surface. A thin layer therefore samples only part of the near field, and its refractive-index sensitivity approaches the bulk value as t becomes large relative to L_d.

The importance of analyte–mode overlap can also be expressed through first-order electromagnetic perturbation theory [87]. For a small dielectric perturbation at fixed resonator geometry, within the lossless and nondispersive bound-mode approximation,

$$\frac{\Delta\lambda}{\lambda_0} \approx \frac{1}{2}\frac{\int \Delta\varepsilon(r)\,|\,E_0(r)\,|^2 dV}{\int \varepsilon(r)\,|\,E_0(r)\,|^2 dV} \tag{7}$$

where $\Delta\lambda$ is the resonance-wavelength shift, λ_0 is the unperturbed resonance wavelength, $E_0(r)$ is the unperturbed electric field, $\varepsilon(r)$ is the permittivity distribution, and $\Delta\varepsilon(r)$ is the analyte-induced permittivity change. Both volume integrals are evaluated over the same unperturbed modal domain, with $\Delta\varepsilon$(r) equal to zero outside the analyte-perturbed region. The numerator represents the spatial overlap between the analyte-induced dielectric perturbation and the modal electric field, whereas the denominator provides the corresponding electromagnetic-mode normalization. Sensor design should therefore maximize the overlap between accessible analyte regions and regions of strong field intensity. Dispersive, absorptive, strongly radiating resonances, or perturbations involving shifts in high-index-contrast material boundaries require an appropriate extension of this first-order approximation.

Reference-channel measurements can further improve readout stability by compensating for shared environmental fluctuations, as demonstrated in self-referenced optical biosensing [88]. When the sensing and reference channels experience comparable common-mode perturbations, a differential wavelength signal can be defined as

$$D = \Delta\lambda_s - \Delta\lambda_r \tag{8}$$

where D is the differential wavelength signal, and $\Delta\lambda_s$ and $\Delta\lambda_r$ are the wavelength shifts in the sensing and reference channels, respectively. The reference channel should minimize specific target binding while experiencing the relevant environmental and instrumental perturbations. Effective cancellation by direct subtraction requires closely matched wavelength responses to these shared perturbations. If the channel responses differ, subtraction provides only partial compensation, and the mismatch should be characterized through calibration. Residual differential noise and drift should therefore be quantified under the intended assay conditions.

2.3. Metasurface Material Systems

Representative material platforms and their roles in metasurface sensing are summarized in Figure 4. These categories overlap; functional materials are grouped by their sensing roles rather than dimensionality alone.

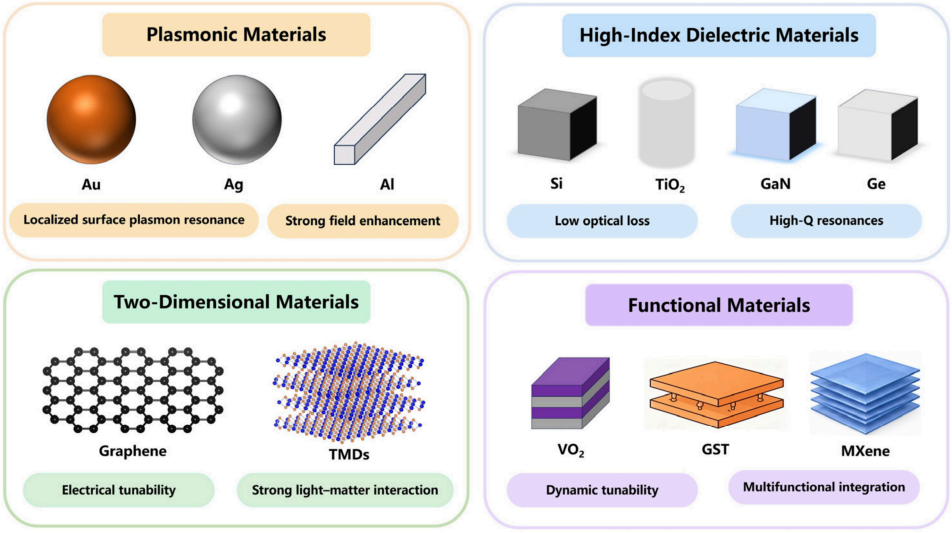


Figure 4. Representative material platforms and their roles in metasurface-enhanced sensing. Material icons are schematic.

2.3.1. Plasmonic Materials

Plasmonic materials, including gold (Au), silver (Ag), and aluminum (Al), underpin metallic metasurfaces. Their complex permittivity, together with structural geometry and the surrounding dielectric environment, governs LSPR positions, linewidths, and local-field enhancement [89–92].

Au remains widely used because it combines chemical stability with established surface-functionalization and nanofabrication methods, making it suitable for biosensing, SERS, and refractive-index sensing in the visible and near-infrared regions [93,94]. Ag generally exhibits low optical loss in the visible range, supporting strong local-field enhancement and relatively narrow plasmonic resonances; however, its susceptibility to surface chemical degradation can limit long-term stability [95]. Al is attractive for ultraviolet plasmonics because of its high plasma frequency, but its native oxide layer changes the interfacial dielectric environment and may complicate surface functionalization and sensing stability [91,96].

Other material options include copper (Cu), magnesium (Mg), doped semiconductors, transparent conducting oxides, and transition-metal nitrides [92]. TiN combines thermal stability with processing compatibility, although optical losses, surface roughness, and film quality still require careful consideration [97]. Material selection should balance spectral performance, chemical stability, and fabrication compatibility. Metal–dielectric hybrid structures and low-loss coupled modes offer routes to combine local-field enhancement with spectral resolution [89,90,92].

Recent numerical studies have explored six-, triple-, and four-band AlCuFe-based terahertz (THz) absorbers [98–100]. These designs demonstrate geometry-dependent resonance tuning and refractometric responses. Their analytical applicability still requires experimental validation of analyte-specific detection, fabrication reproducibility, and performance in realistic samples.

2.3.2. High-Refractive-Index Dielectric Materials

To reduce the ohmic losses and nonradiative dissipation associated with metallic plasmonic materials, high-refractive-index dielectrics have become important material platforms for metasurface sensing. Materials such as Si, TiO_2, GaN, and Ge can support electric-dipole, magnetic-dipole, and higher-order multipolar Mie resonances. Within appropriate spectral windows, their high refractive indices and relatively low absorption losses provide favorable conditions for achieving narrow linewidths and high-Q resonances [57,101,102]. However, the actual Q factor is also governed by radiative leakage, modal coupling, and structural symmetry.

Si is widely used for near-infrared dielectric metasurfaces and supports the design of Mie, Fano, and BIC/quasi-BIC resonances [103]. TiO_2 combines a high refractive index, a broad transparency window, and good chemical stability, making it attractive for dielectric metasurfaces and optical biosensing [57,102]. GaN provides a low-loss platform for visible-light metasurfaces and offers opportunities for integrated nanophotonic devices [104]. Ge is particularly suitable for mid-infrared dielectric metasurfaces, where its optical properties enable resonant field control and molecular spectroscopic sensing [101]. Material selection should therefore consider the operating wavelength, absorption loss, refractive index, analyte access to the resonant field, and fabrication tolerances, especially for high-Q structures.

2.3.3. Two-Dimensional Materials

Two-dimensional materials combine atomic-scale thickness, high surface-to-volume ratios, and tunable electronic properties, enabling their use as optical modulation layers and sensing interfaces [105,106]. Their optical and electronic responses are sensitive to molecular adsorption, charge transfer, and changes in the surrounding dielectric environment.

Graphene supports tunable plasmonic modes in the mid-infrared and terahertz regions. Its Fermi level can be controlled through electrical gating, electrochemical doping, or chemical functionalization [105]. Integration with metallic or dielectric metasurfaces combines local-field enhancement with tunable resonance and absorption responses, supporting applications in mid-infrared molecular fingerprinting and refractive-index sensing [107,108].

As a recent design example, Zha and Cheng numerically investigated a patterned graphene absorber with five mid-infrared resonances and wavelength sensitivities of approximately 931–1134 nm/RIU [109]. The work illustrates multichannel refractometric design and tunability through graphene parameters. However, the calculated responses to changes in the surrounding refractive index should be distinguished from selective molecular recognition and experimentally calibrated chemical sensing.

Transition-metal dichalcogenides (TMDs), including MoS_2, WS_2, and WSe_2, exhibit strong excitonic responses in the visible and near-infrared regions [106,110]. The optical response of these materials is sensitive to layer number, carrier concentration, defect population, and the surrounding dielectric environment. This tunability supports sensing strategies based on defect engineering and heterostructure design. When TMDs are combined with metallic nanostructures, Raman signals can benefit from both plasmonic near-field enhancement and interfacial charge transfer. Under suitable spectral overlap, excitonic resonances may provide an additional contribution to the overall enhancement [111]. Violet phosphorus has also been explored as a fluorescence quencher and a component of charge-transfer-assisted SERS substrates, as reviewed by Nawaz et al. [112].

Reproducible sensing therefore depends on controlling layer number, defect density, interface cleanliness, and material uniformity during preparation and integration. Recent analysis of two-dimensional heterostructures identifies transfer-induced contamination, growth-related defects, and integration constraints as important sources of device variabil-

ity [113]. For metasurface sensing, these factors can alter carrier density, optical loss, charge transfer, and recognition-layer attachment. The advantages of a hybrid interface should consequently be assessed together with chip-to-chip variability and stability after exposure to the intended sample matrix.

2.3.4. Functional Materials

Phase-change materials provide a means of tuning resonances during operation by altering their dielectric response [114,115]. Functional materials at the interface serve a complementary role by influencing analyte adsorption and local enrichment around metasurface resonators.

Vanadium dioxide (VO_2) and germanium–antimony–tellurium (GST) are representative examples. VO_2 changes its dielectric response through a reversible insulator–metal transition, whereas GST provides nonvolatile multistate control through crystalline–amorphous phase changes. When incorporated into metasurface resonators, these materials can shift resonances, switch sensing modes, and adjust spectral overlap with target analytes [115,116]. Their practical implementation also depends on transition temperature, switching energy, cycling stability, thermal crosstalk, and fabrication compatibility.

Beyond VO_2 and GST, Chen et al. demonstrated laser-written In_3SbTe_2 phase-change metasurfaces for infrared and terahertz polarization control [117]. Crystalline patterns embedded in an amorphous matrix provide an experimentally demonstrated route to programmable optical responses and large-area fabrication. Although this study did not establish chemical or biological sensing performance, its fabrication approach is relevant to reconfigurable illumination and polarization-resolved readout. Its use in sensing would additionally require assessment of switching-induced heating, baseline stability, and compatibility with functionalized interfaces.

MXenes, a family of two-dimensional transition-metal carbides, nitrides, and carbonitrides, provide surface terminations that can promote analyte adsorption, local enrichment, and interfacial charge transfer [118,119]. Coordination, electrostatic interactions, and hydrogen bonding with analytes can change the local dielectric environment and charge distribution, thereby altering SPR, LSPR, and SERS responses. Surface chemistry, oxidation, and batch-to-batch variation must be controlled to preserve adsorption capacity, long-term stability, and sensing reproducibility.

Material selection should begin with the analyte, sample medium, and required spectral window. Plasmonic structures are attractive when strong fields must be concentrated near small molecules or catalytic interfaces, but absorption losses, surface degradation, and photothermal perturbations may limit performance. Low-loss dielectric structures favor narrow resonances and reduced dissipative heating, provided that a sufficient fraction of the mode remains accessible to the analyte. Two-dimensional materials can add tunability and chemically responsive interfaces, while hybrid architectures combine these functions at the cost of additional fabrication and interfacial variability [42,116,117].

Analyte dimensions provide a further selection criterion. Thin molecular layers require substantial surface-field overlap, whereas vesicles and cells may benefit from spatially extended fields or structures that bring their relevant components close to the sensing region. For low refractive-index contrast, narrow linewidths are useful only if spectral contrast, referencing, and environmental stability permit small shifts to be resolved. Long-term measurements in aqueous or outdoor environments place greater weight on surface chemistry and coating stability than on peak calculated enhancement. Table 1 summarizes these trade-offs as a material-selection guide rather than a universal ranking.

Table 1. Material-selection considerations for metasurface-enabled sensing.

Platform	Useful Spectral Range	Favorable Sensing Requirements	Main Limitations	Selection Priority
Plasmonic metals	Ultraviolet to infrared, depending on metal and geometry	Strong surface fields; vibrational spectroscopy; small molecules; catalytic interfaces	Dissipative loss, heating, oxidation or corrosion, hotspot variability	Balance field confinement with chemical stability and analyte access
High-index dielectrics	Visible to mid-infrared within material transparency windows	Narrow resonances; small spectral shifts; reduced dissipative heating	Fabrication sensitivity; inaccessible internal fields; angular dependence	Optimize accessible-field overlap and measurable resonance contrast
Two-dimensional material interfaces	Material-dependent; graphene is particularly relevant to mid-infrared and THz operation	Electrical tunability; adsorption and charge-transfer responses; thin functional interfaces	Transfer contamination, defects, oxidation, carrier-density variability	Verify interface uniformity and stability in the intended matrix
Metal–dielectric and other hybrids	Architecture-dependent	Combined field localization, spectral selectivity, and interfacial functionality	More complex fabrication and cross-interface variability	Demonstrate an analytical benefit over simpler reference structures
Phase-change and reconfigurable systems	Infrared and THz in representative platforms	Adjustable spectral or polarization response	Switching heat, hysteresis, cycling stability, calibration changes	Separate reconfiguration performance from analyte detection performance

3. Metasurface-Enhanced Chemical Sensing

Chemical sensing encompasses gases and volatile molecules, liquid-phase analytes, and catalytic intermediates. Key limitations are weak responses and limited surface residence in gases [32,120–122], solvent and matrix backgrounds [123,124], and low-coverage, short-lived catalytic intermediates [31,125–129]. The discussion below focuses on how resonant enhancement, selective interfaces, and sample transport address these constraints.

3.1. Gases and Volatile Small Molecules

3.1.1. Trace Gas Detection Using High-Q Resonances and Selective Enrichment

Compact gas sensors must resolve weak responses from analytes with limited surface residence. Narrow resonances improve the resolution of small refractive-index or absorption changes, while selective adsorption layers enrich molecules within accessible near fields. Their combined benefit depends on analyte–mode overlap and interfacial selectivity.

For CO_2 sensing, He and Ma proposed a tungsten THz metasurface with asymmetric cross-shaped apertures supporting two quasi-BIC modes generated by symmetry breaking [120]. A polyhexamethylene biguanide (PHMB) layer was added to capture CO_2. Numerical calculations predicted a frequency-shift sensitivity of 0.06 GHz/ppm and a theoretical detection limit of approximately 33.3 ppm. Ghanim et al. studied PHMB-coated silver bowtie and fan-shaped nanoantennas, modeling their spectral responses over 0–524 ppm through a relationship between the PHMB refractive index and CO_2 concentration [122]. Both designs combine resonant enhancement with analyte capture, but their concentration responses are based on numerical simulations and functional-layer models.

Direct calibration under gas exposure, together with tests of temperature and humidity effects, cross-sensitivity, and long-term stability, is still needed.

Tuning the material itself provides another way to adjust the operating window. A numerical study of methylammonium lead iodide ($MAPbI_3$) quasi-BIC metastructures demonstrated temperature-dependent resonance tuning and assessed their potential for CO_2 sensing [130]. Their performance under practical gas-sensing conditions has yet to be established.

For methane, an experimental concentration calibration has also been reported. In a 2025 study, symmetry breaking in an all-dielectric high-Q Fano metasurface generated multiple narrow resonances. Methane exposure produced a concentration-dependent wavelength shift of approximately −1.03 nm/% [37]. This result establishes a direct link between methane concentration and spectral response rather than relying solely on changes in the background refractive index. The usable concentration range, humidity tolerance, and low-concentration detection performance still require further assessment.

Selective enrichment has also been combined with high-Q resonances for trace volatile organic compound (VOC) detection. Zhang et al. integrated polyvinylpyrrolidone (PVP) with a nonlocal terahertz metamaterial supporting multiple quasi-BIC resonances. Hydrogen-bonding and van der Waals interactions promoted interfacial adsorption and enrichment, with reported limits of detection (LODs) of approximately 12.2, 8.2, and 9.1 ppb for acetone, isoamyl alcohol, and ethyl acetate, respectively, in controlled room-temperature gas experiments [131]. The molecule-dependent responses highlight the contribution of analyte enrichment and analyte–field overlap to chemical discrimination.

3.1.2. Multichannel Spectral Responses and Molecular Fingerprint Analysis

A resonance shift alone offers limited discrimination when volatile compounds produce similar dielectric perturbations. Multiband resonances, molecular absorption fingerprints, and data-driven analysis provide complementary information for gas identification.

Wang et al. numerically investigated a multiband terahertz absorber integrated with microfluidic channels, obtaining a maximum refractive-index sensitivity of approximately 400 GHz per RIU over an analyte refractive-index range of 1.3–1.4 [132]. This design provides a multichannel refractometric response, although its relevance to gas-phase VOC detection requires validation using realistic gas optical properties and concentration-dependent measurements.

Electrically tunable graphene metasurfaces provide design strategies that may be transferable to gas sensing. Zhao and Wang numerically investigated quasi-BIC-enhanced terahertz fingerprint sensing of lactose and tyrosine thin films [133], while Khafagy et al. modeled tunable multiband refractometric responses [134]. These studies illustrate resonance tunability, but do not establish gas-phase detection or discrimination.

Multidimensional spectral responses can also be combined with data-driven methods for gas identification. Wertani et al. used refractive-index values corresponding to CO_2, CH_4, N_2, C_3H_8, and air to simulate the responses of a graphene terahertz metasurface, then applied random forest regression to predict resonance characteristics [135]. This work demonstrates the potential of data-assisted design and spectral prediction, but experimental classification under actual gas exposure, mixed-gas conditions, and previously untested operating conditions remains to be established.

Meng et al. developed a temperature-stabilized mid-infrared gas-sensing system operating at 7–14 μm, as shown in Figure 5a [136]. Its metasurface filter array uses gold square rings and complementary ring-shaped apertures to provide bandstop and bandpass channels. The system classified CO_2 and CH_4 at 10–100%, NH_3 at 100–1000 ppm, and methyl ethyl ketone (MEK; 2-butanone) at 200–400 ppm, using N_2 as the reference. An

independently acquired hold-out dataset yielded class-specific true-positive rates of 100% for CO_2, CH_4, and NH_3 and 94.4% for MEK, with an overall classification accuracy of 98.4% [136]. The class-specific true-positive rate describes the fraction of samples from a given class correctly assigned to that class, whereas overall accuracy describes the fraction of all test samples correctly classified. These results support classification within the tested concentration ranges; they do not establish quantitative analysis of multicomponent gas mixtures.

In a numerical study, Álvarez-Sanchis et al. examined a free-standing silicon Huygens metasurface supporting electric- and magnetic-dipole quasi-BIC resonances [121]. The two responses were balanced under the Kerker condition, and the resonances were aligned with characteristic absorption frequencies of hydrogen cyanide (HCN) and sulfur dioxide (SO_2), thereby enhancing gas absorption. Chemical discrimination with this approach depends on molecular absorption fingerprints, whereas its performance under controlled gas exposure still requires experimental validation.

3.1.3. Reliability and Practical Limitations in Complex Gas Environments

Reliable gas sensing requires response and recovery times, cycling tests, device-to-device statistics, batch reproducibility, interfering-gas measurements, and calibration under changing temperature and humidity [32]. The practical advantage of narrow quasi-BIC resonances is reduced when fabrication variability or environmental drift becomes comparable to the target-induced response. Multichannel classification additionally requires representative datasets and independent test data.

Many CO_2 platforms remain numerical [120,122,130], whereas methane, VOC, and multichannel classification studies include gas-exposure experiments [37,131,136]. Validation priorities are realistic mixtures, combined temperature–humidity variation, and long-term measurements across independent devices and batches.

3.2. Liquid-Phase Molecular Recognition and Complex Matrix Analysis

3.2.1. Microfluidic Confinement and Enhanced Terahertz Dielectric Responses

Strong water absorption suppresses THz resonances, limiting the value of high refractive-index sensitivity alone [123,137]. Microfluidic confinement reduces liquid thickness and controls analyte delivery, but effective sensing also requires accessible near fields and resistance to nonspecific adsorption.

MoradiFotouhi and Pourfath integrated monolayer graphene strips and gold rods within a microfluidic channel, exploiting bright–dark mode coupling to produce plasmon-induced transparency (PIT). Simulations yielded a refractive-index sensitivity of approximately 700 GHz/RIU over an index range of 1.33–1.43 [137]. An effective refractive-index model was also used to explore the detection of glucose and other analytes. However, without measurements on actual liquid samples, this study provides a numerical proof of concept for combining microfluidic confinement with PIT-enhanced sensing.

To address water absorption, Cao et al. integrated an ultrathin microfluidic channel with a sandwich-type terahertz metasurface, enhancing the resonant response in aqueous solutions by reducing liquid thickness and improving near-field overlap [123]. This approach directly addresses a practical limitation of terahertz liquid sensing. Related design studies have explored multilayer terahertz resonators with deep-learning optimization [138] and graphene–$Ti_3C_2T_x$ terahertz metasurfaces with machine-learning-assisted analysis [139]. Metal–insulator–metal (MIM) nanoring sensors have also been investigated numerically at infrared wavelengths [140]. For numerical proposals, predicted refractive-index responses should be distinguished from experimentally validated detection in actual liquid samples.

Reducing the liquid-layer thickness improves optical access but does not necessarily ensure rapid analyte delivery to the sensing surface. Under laminar flow, convection mainly transports analytes along the channel, while diffusion remains important across the near-wall boundary layer. When surface binding consumes analytes faster than they are replenished, the local concentration falls below the bulk concentration and the measured association kinetics become transport-limited [141]. The relative roles of convection and diffusion can be characterized by the Péclet number, $Pe = Uh/D$, where U is the characteristic flow velocity, h is the channel height, and D is the analyte diffusion coefficient. For an initially unsaturated binding interface, the surface Damköhler number can be expressed as $Da = k_{on}\Gamma_{max}h/D$, where k_{on} is the association rate constant, and Γ_{max} is the maximum surface binding-site density. This dimensionless number compares the characteristic surface reaction rate with diffusion across the channel height.

Increasing flow can reduce boundary-layer depletion, but also increases sample consumption and may reduce residence time or impose damaging shear on biological samples. Moreover, rapid flow above a nanostructure does not guarantee analyte entry into recessed nanogaps. Flow-through architectures, local mixing, and active transport should therefore be evaluated by capture efficiency, delivered analyte amount, and time to a stable response, together with channel dimensions, flow rate, and total sample volume.

3.2.2. SERS Molecular Fingerprinting and Analysis of Complex Food Matrices

SERS fingerprints can support chemical identification, but real-sample quantification also depends on hotspot access, adsorption, and matrix backgrounds. Spike recovery, batch-to-batch reproducibility, regenerability, and storage stability complement detection limits measured in standard solutions.

Zhu et al. developed nanoporous silver structures with dense SERS hotspots, achieving an LOD of approximately 1×10^{-7} M (24 ppb) for thiram. Reusability was demonstrated over 60 successive detection–regeneration cycles using 10 μM phosmet, with each regeneration involving 4 h of ethanol washing under continuous stirring [142].

For complex food matrices, Singh et al. developed an aptamer-functionalized SERS microarray based on silver-coated porous silicon (Ag-pSi). As shown in Figure 5b, the array was modified with aptamers and 5,5′-dithiobis(2-nitrobenzoic acid) (DTNB) and interrogated using 785 nm excitation. Target binding produced a concentration-dependent decrease in the normalized DTNB reporter signal at 1341 cm^{-1}, enabling indirect "signal-off" quantification of the mycotoxins [143]. Calibration curves for aflatoxin B_1 (AFB_1), fumonisin B_1 (FB_1), and ochratoxin A (OTA) yielded coefficients of determination (R^2) of 0.99, 0.99, and 0.98, respectively. The authors reported LODs of 0.008, 0.547, and 0.922 ppb for AFB_1, FB_1, and OTA, respectively. Tests using spiked wheat, maize, and rice samples yielded recoveries of 95–104%, with reported relative standard deviations (RSDs) of 1.5–6.6% across the tested sample–analyte combinations [143]. These values characterize precision in the spiked-sample measurements and should not be interpreted as independent fabrication-batch reproducibility.

Spectroscopic data fusion offers a complementary route to more robust quantification. For example, combining near-infrared spectra with SERS features can improve regression-based prediction of pesticide residues by exploiting complementary spectral information [144]. Such approaches provide additional analytical information when variable matrix backgrounds limit quantification based on a single characteristic band.

3.2.3. Mid-Infrared Spectral Encoding and Complex Matrix Analysis

Mid-infrared vibrational fingerprints provide molecular information beyond bulk refractive-index shifts. Resonant enhancement and spectral encoding address weak absorp-

tion, limited spectral coverage, and overlapping bands, while enabling compact readout of complex liquid samples.

Chen et al. developed a chip-scale mid-infrared spectroscopy platform using metasurface-engineered thermal emitters, low-cost detectors, and classification algorithms to distinguish solvents and pharmaceutical compounds [145]. By using predefined spectral channels for encoded readout, this approach reduces reliance on scanning spectrometers and supports miniaturized chemical analysis. Here, the metasurface controls the source emission spectrum, while analyte identification relies on far-field absorption measurements.

In 2025, Rosas et al. reported a scalable gradient plasmonic microhole array for surface-enhanced infrared absorption spectroscopy (SEIRAS). Approximately 400 sensor chips could be fabricated on a 6-inch wafer, while a continuous gradient in structural parameters produced more than 400 narrowband resonances spanning the molecular fingerprint region of 1200–2000 cm^{-1} [124]. To evaluate performance with complex biological samples, filtered human peritoneal fluid was spin-coated onto the metasurface and dried at room temperature for 5 h before infrared measurements. Infrared imaging at 1656 cm^{-1} indicated a relatively uniform sample distribution, and the SEIRAS spectra resolved the amide I and amide II bands near 1656 and 1546 cm^{-1}, respectively. The amide I absorption signal reached approximately 40% on the metasurface, compared with 2% on a reference CaF_2 substrate, corresponding to an approximately 20-fold enhancement.

The study combined broad fingerprint coverage with wafer-scale fabrication and tested films prepared from biofluids collected from real biological samples. In a complementary numerical study, Gao et al. used neural-network-based inverse design to tailor terahertz metasurface resonances for selected plant-related molecules [146]. Together, these efforts reflect a move toward multiresonant platforms, wider fingerprint coverage, and data-assisted interpretation. Their practical value, however, still needs to be established using independent samples and measurements from multiple devices.

3.3. Catalytic Interface Reactions and In Situ Spectroscopic Monitoring

Studies using periodic metasurfaces for in situ catalytic monitoring remain relatively limited. This section therefore also considers plasmonic nanostructures with engineered coupling between optical hotspots and catalytic active sites. These related platforms illustrate transferable principles for interface design and in situ readout, while remaining distinct from planar metasurfaces.

3.3.1. In Situ Enhanced Spectroscopy and Reaction Intermediate Monitoring

Enhanced in situ spectroscopy couples catalytic interfaces to strong optical fields, allowing low-coverage and transient intermediates to be monitored under reaction conditions [125,126]. Metasurfaces and related plasmonic structures can combine catalytic sites with time-resolved spectroscopic readout [127,128].

Lu et al. developed a bifunctional structure comprising Au nanorods decorated with Pd nanoislands (AuNR@Pd islands). The Au nanorods provided localized plasmonic fields for SERS enhancement, while the Pd nanoislands supplied catalytic sites for the $NaBH_4$-mediated reduction of 4-nitrothiophenol (4-NTP) [127]. As shown in Figure 5c, this architecture combined catalysis and spectroscopic readout at the same interface. During the 0–180 s reaction period, the 4-NTP bands associated with nitro groups (R–NO_2) progressively decreased, while bands associated with amino groups (R–NH_2) in the product, 4-aminothiophenol (4-ATP), emerged and intensified. The spectral evolution directly tracked reactant-to-product conversion, showing that spatially colocating enhanced optical fields and catalytic sites enables time-resolved reaction monitoring. Related Au–Ag alloy nanoshells have also been used for time-resolved SERS measurements [129].

The approach has also been applied to electrocatalytic interfaces. Hao et al. used in situ SERS to compare CO_2 reduction on Au@Pd bimetallic structures with Pd configurations ranging from isolated atoms to a monolayer [128]. Changes in intermediate spectra provided insight into how Pd site configurations influence reaction pathways, linking structural differences to surface intermediates and reaction selectivity.

Multiband SEIRA provides a complementary means of probing adsorbed reaction intermediates. Duportal et al. developed two Pt metasurface arrays targeting linearly adsorbed CO near 2030 cm^{-1} and bridge-bonded CO near 1840 cm^{-1}. Both configurations were resolved in CO-saturated electrolyte (Figure 5d). During CO_2 electroreduction in K_2CO_3 electrolyte, linearly adsorbed CO was detected, whereas no bridge-bonded CO signal was resolved under the reported conditions. In the CO-saturated measurements, the high-frequency array provided an approximately 40-fold enhancement of the linearly adsorbed CO signal relative to an unstructured Pt reference film. Enhancement of the bridge-bonded CO signal could not be reliably quantified because its reference signal on the unstructured film was not clearly resolved [147]. Spectrally targeted enhancement therefore enables different CO adsorption configurations to be resolved under specified reaction conditions.

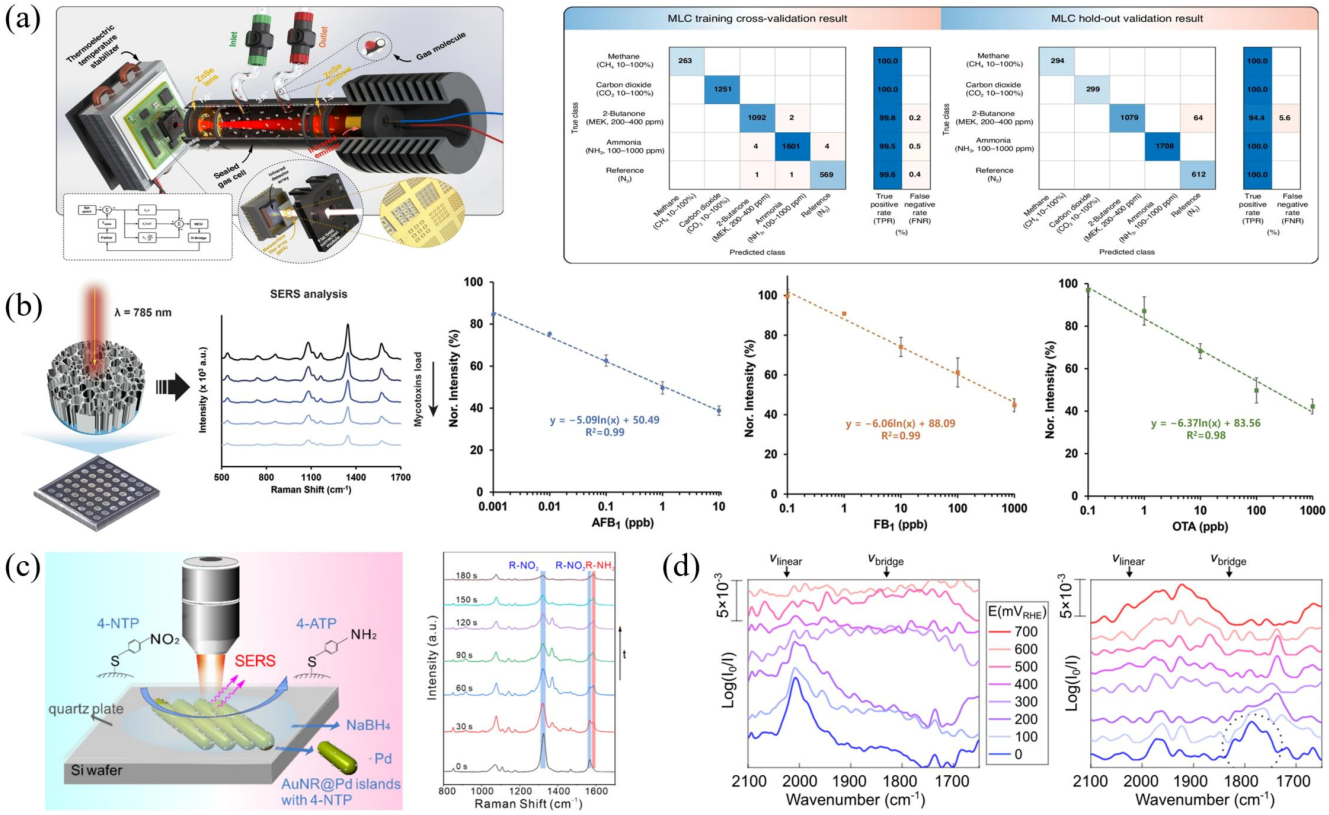


Figure 5. Representative metasurface-based and related nanostructured platforms for chemical sensing and in situ catalytic monitoring. (**a**) Multichannel mid-infrared metasurface for CH_4, CO_2, MEK, and NH_3 discrimination (adapted from [136], 2024). (**b**) Aptamer-functionalized Ag-coated porous-Si SERS array for multiplexed detection of AFB_1, FB_1, and OTA (adapted from [143], 2025). (**c**) Au-nanorod@Pd-island substrate for SERS monitoring of 4-NTP reduction to 4-ATP (adapted from [127], 2025). (**d**) SEIRA monitoring of linearly adsorbed and bridge-bonded CO on Pt metasurfaces (adapted from [147], 2024).

3.3.2. Coupling Between Optical Enhancement and Catalytic Modulation

The role of an enhancing structure in catalytic measurements depends on whether illumination primarily provides spectroscopic readout or also changes the reaction. In a minimally perturbative measurement, the metasurface enhances signals from intermediates while the reaction rate and product distribution remain insensitive to the probe under the selected conditions. In an actively illuminated catalytic system, plasmon decay can generate nonequilibrium carriers or heat, and interfacial charge transfer can modify adsorption and reaction pathways [148–153]. Strong field gradients may also redistribute polarizable species or alter local mechanical conditions, but such effects require evidence specific to the structure and reaction.

Photoresponsive Ag/TiO_2 structures illustrate this coupling because illumination can contribute to charge-transfer-assisted Raman enhancement and photocatalytic regeneration [154,155]. Plasmon-free atomic-scale SERS platforms provide a complementary example in which charge transfer contributes to both spectroscopic response and photocatalytic monitoring [156]. In either case, an illumination-dependent spectral change cannot by itself establish whether the dominant origin is altered scattering efficiency, changing intermediate coverage, photochemical conversion, or heating.

Mechanistic interpretation requires dark measurements, probe-power series, and off-resonance controls, together with matched-temperature dark experiments where photothermal effects are plausible. Wavelength-dependent reaction rates or action spectra should be compared under appropriately normalized photon flux or absorbed power. Off-resonance illumination alone does not isolate nonthermal effects because optical absorption and heating also change with wavelength. Independent product analysis, suitable noncatalytic or nonplasmonic reference structures, and characterization before and after illumination further help separate signal enhancement from reaction modification. The probe conditions should be reported, and a weakly perturbative operating regime should be established whenever the aim is to observe intrinsic reaction kinetics.

3.4. Summary

Across gas sensing, liquid-phase analysis, and catalytic monitoring, performance depends on coordinated resonator design, interfacial selectivity, sample transport, and readout rather than optical enhancement alone. Table 2 compares representative strategies, results, validation conditions, and key limitations.

Table 2. Representative chemical sensing strategies, validation status, and key limitations.

Application	Main Strategies	Representative Results	Validation Status	Key Limitations
Gases and VOCs	High-Q/quasi-BIC resonances; selective enrichment; multichannel fingerprinting	CO_2 sensitivity: 0.06 GHz/ppm (simulated) [120]; ppb-level VOC detection [131]; hold-out class-specific true-positive rates: 94.4–100% [136]	Simulations [120,122]; CH_4/VOC exposure experiments [37,131]; single-gas classification [136]	Temperature/humidity interference; cross-sensitivity; mixture discrimination; drift
Liquid-phase analytes and complex matrices	Microfluidic confinement; selective SERS; broadband SEIRAS	Reported mycotoxin LODs: 0.008–0.922 ppb; spike recoveries: 95–104%; assay RSDs: 1.5–6.6% [143]; infrared enhancement: ≈20× [124]	Numerical study [137]; aqueous solutions [123]; spiked food extracts [143]; dried biofluid films [124]	Nonspecific adsorption; substrate variability; sample standardization
In situ catalytic monitoring	Hotspot engineering; time-resolved SERS; multiband SEIRAS	Reaction tracking over 0–180 s [127]; linear-CO signal enhancement: ≈40× [147]	Model catalytic reactions [127–129]; in situ electrochemical CO measurements [147]	Intermediate assignment; mechanism discrimination; quantitative kinetics

The main validation gaps are gas-mixture discrimination and environmental drift, solvent backgrounds and substrate variability, and independent verification of intermediate assignments and reaction kinetics. Application-specific tests and comparisons with established reference methods remain essential.

4. Metasurface-Enhanced Biosensing

Biosensing targets range from small molecules and nucleic acids to proteins, vesicles, microorganisms, and living cells [43,157–159]. Across these target scales, the discussion considers optical transduction, recognition interfaces, sample handling, and validation in real samples.

4.1. Detection of Small Molecules and Nucleic Acids

4.1.1. Small Molecules

Small metabolites, hormones, vitamins, and drugs often produce weak binding-induced refractive-index changes. Liquid chromatography–tandem mass spectrometry (LC–MS/MS) provides specific quantification but requires specialized instrumentation; immunoassays and SPR depend strongly on recognition affinity and transduction efficiency. Metasurface designs must therefore provide target specificity through selective capture or distinctive molecular fingerprints, together with a sufficient optical signal-to-noise ratio [158,160,161].

Refractometric platforms combine localized field enhancement with specific recognition interfaces to improve the detection of small-molecule binding. Cusano et al. demonstrated label-free detection of 25-hydroxyvitamin D_3 [25(OH)D_3] using a plasmonic metasurface, obtaining responses over clinically relevant concentration ranges in complex matrices [162]. Fan et al. developed a platform with smartphone readout for simultaneous, sample-to-answer detection of testosterone and 25(OH)D_3 in diluted whole blood [163]. These studies illustrate the development of fiber-optic probes and portable integrated systems, respectively. They also highlight the importance of recognition-layer design and spatial overlap between analytes and enhanced near fields, alongside the resonance Q factor, for detecting low-molecular-weight targets.

For continuous metabolite monitoring, Li et al. modified a metasurface plasmon resonance (MetaSPR) chip with a MXene–graphene oxide (GO) functional layer and immobilized glucose oxidase. As shown in Figure 6a, sensing and reference chips were integrated into a dual-channel microfluidic platform to record real-time responses to different glucose concentrations in artificial sweat under continuous flow [164]. Combining enzymatic recognition with reference correction helps improve selectivity and reduce matrix interference. Long-term monitoring nevertheless requires further evaluation of enzyme activity retention, immobilized-layer stability, and baseline drift.

A related fiber-integrated plasmonic array was reported by Li et al., who combined an arrayed silver resonant-cavity structure with a two-dimensional Cu-TCPP metal–organic framework (MOF) on a plastic optical fiber [165]. Following glucose oxidase immobilization, the sensor exhibited a wavelength sensitivity of 9.99 nm/(mg/mL) over a glucose concentration range of 0.1–1.2 mg/mL.

THz quasi-BIC and broadband-enhancement platforms have detected L-glutamic acid and resolved L-tyrosine fingerprints, respectively [166,167]. These model-system studies demonstrate enhanced vibrational readout, but water absorption and complex biofluid backgrounds still limit translation to dilute biological samples.

SERS platforms have further advanced toward complex biofluid analysis and continuous monitoring. Zheng et al. combined a gold nanopyramid metasurface featuring relatively uniform hotspots with a neural network to distinguish and quantify clozapine

and its metabolites in serum over concentration ranges relevant to therapeutic drug monitoring [168]. Wang et al. integrated a silver nanocube SERS substrate with a module for iontophoretic sweat induction in a flexible wearable patch, enabling noninvasive tracking of nicotine concentration changes through SERS measurements of sweat [169]. These studies highlight compatibility with complex matrices, continuous sampling, and data interpretation as key capabilities for practical biosensing.

4.1.2. Nucleic Acids

Nucleic acid sensing requires low-concentration detection and mismatch discrimination. Polymerase chain reaction (PCR) and quantitative PCR (qPCR) provide high sensitivity through target amplification. Metasurface-based assays support both direct hybridization detection and optical readout coupled to target or signal amplification [170,171].

High-Q resonances facilitate amplification-free detection by resolving small interfacial changes induced by nucleic acid hybridization. Hu et al. immobilized deoxyribonucleic acid (DNA) probes on a single-crystalline silicon metasurface supporting guided-mode resonances for amplification-free, label-free detection of severe acute respiratory syndrome coronavirus 2 (SARS-CoV-2) gene fragments. As shown in Figure 6b, complementary targets produced concentration-dependent resonance wavelength shifts, whereas noncomplementary sequences generated weaker responses. The platform exhibited an average Q factor of approximately 2200 and a detection limit of approximately 8 fM in physiological buffer. A discernible response was obtained within approximately 5 min after spiking 100 nM target sequences into SARS-CoV-2-negative nasopharyngeal swab eluates [172]. These results demonstrate the potential of high-Q dielectric metasurfaces for rapid, direct nucleic acid detection. However, the detection limit achieved in buffer cannot be directly extrapolated to clinical samples, and performance at low target concentrations in complex matrices requires further validation.

Molecular amplification can also be coupled to nanophotonic readout. As a related nanoplasmonic example, the clustered regularly interspaced short palindromic repeats (CRISPR)-Cas chiral biosensor (CENSOR) platform integrates CRISPR–Cas13a recognition, DNA origami assembly, and chiral optical readout. Following target preamplification, it achieved a calculated detection limit of 0.133 aM and underwent small-scale validation using clinical nasopharyngeal swab samples [173]. Flexible THz metamaterials have also been paired with rolling circle amplification (RCA) to detect hepatitis B virus (HBV) DNA in patient serum [174]. Although RCA improves analytical sensitivity, it introduces additional amplification and handling steps, increasing procedural complexity.

Liquid-biopsy applications place particular demands on sequence specificity and tolerance to complex matrices. Luo et al. addressed these requirements with a metal–graphene hybrid THz metasurface that combined hybridization chain reaction (HCR) with nanoparticle-mediated charge modulation, providing two modes of signal amplification for detecting circulating tumor DNA (ctDNA) carrying the *KRAS* G12D mutation. The assay reached a detection limit of 0.22 fM and distinguished single-nucleotide mismatches. Results from plasma samples obtained from 12 patients with pancreatic cancer and 12 healthy controls showed strong agreement with qPCR results [175]. The study supports the use of metasurfaces for mutation analysis in plasma when combined with nucleic acid signal amplification, although larger clinical cohorts are still needed for validation.

Fluorescence-enhancing metasurfaces primarily improve readout efficiency. Iwanaga used an all-dielectric silicon nanopillar metasurface to enhance microRNA (miRNA) fluorescence, achieving subattomolar detection when combined with reverse-transcription polymerase chain reaction (RT-PCR) [176]. Because these ultralow detection limits were obtained with molecular amplification, they cannot be directly compared with those of

amplification-free platforms; the metasurface contribution lies in improved fluorescence collection and optical readout. Meanwhile, a quasi-BIC THz platform incorporating phenylboronic acid–functionalized gold nanoprobes distinguished let-7a from DNA and was validated in a serum matrix [177], illustrating progress toward selective nucleic acid discrimination in complex samples.

Comparisons should distinguish direct target recognition from target amplification, downstream signal amplification, and physical preconcentration. Label-free optical readout does not necessarily imply an amplification-free assay. For example, the 8 fM LOD reported by Hu et al. was obtained through direct hybridization in buffer [172], whereas the 0.22 fM ctDNA assay combined HCR with nanoparticle-mediated signal amplification [175]. These values characterize different complete workflows and should not be ranked as intrinsic metasurface sensitivities. For each assay, the starting sample volume, dilution or enrichment factor, amplification steps, and total processing time should accompany the reported LOD. Detection limits should also be referenced explicitly to either the original sample or the processed measurement solution.

4.2. Protein Biomarkers

Protein sensing combines established antibody or aptamer recognition with resonant or spectroscopic readout. Comparisons with enzyme-linked immunosorbent assay (ELISA) and chemiluminescence immunoassays should consider sensitivity, assay time, multiplexing, clinical sample size, and agreement with reference measurements [158,178,179].

Tumor biomarker sensing is expanding from highly sensitive single-analyte assays toward clinical validation and combined biomarker assessment. Li et al. developed a nanozyme-enhanced MetaSPR platform (nano-ELISPR). As shown in Figure 6c, nanozyme-catalyzed reactions induce etching of the chip surface, converting immunorecognition into amplified optical responses for separate quantification of alpha-fetoprotein (AFP), carcinoembryonic antigen (CEA), and cancer antigen 125 (CA125). Measurements of 60 clinical serum samples were compared with hospital assay results, showing a strong correlation for CEA (R^2 = 0.961) [180]. Liang et al. combined measurements of prostate-specific antigen (PSA) and the extracellular vesicle-associated marker cluster of differentiation 63 (CD63) to improve prostate cancer diagnosis in patients with PSA levels in the diagnostic gray zone [181]. All-dielectric fluorescence-enhancing platforms, flexible plasmonic structures, and THz metasurfaces have also been explored for detecting PSA, CEA, and midkine [182–184].

Protein sensing for infection and inflammation emphasizes high throughput and comparability with clinical reference methods. Wu et al. developed a MetaSPR platform in a 96-well plate format for simultaneous detection of procalcitonin (PCT), C-reactive protein (CRP), and serum amyloid A (SAA), with quantitative validation in 80 clinical plasma samples. CRP measurements correlated strongly with results obtained by latex-enhanced immunoturbidimetry [185]. This study combined multiplexed, high-throughput, real-time analysis with clinical sample validation, providing evidence beyond analytical detection limits alone. Quasi-BIC THz and three-dimensional SERS platforms have reported responses at lower concentrations in buffer or spiked samples [186,187], but their stability in complex plasma remains less extensively validated.

Cardiovascular and coagulation biomarker sensing places greater emphasis on rapid multiplexed analysis and reliable quantification. Zheng et al. used antigen-binding-induced shifts in the characteristic peaks of Raman reporter molecules as the quantitative SERS readout on an Au/SiO_2 multilayer metasurface, enabling multiplexed detection of creatine kinase-MB (CK-MB), myoglobin (Mb), and cardiac troponin I (cTnI) in serum [188]. Using peak positions helps reduce the influence of intensity variations associated with spatially

nonuniform hotspots. Strongly coupled plasmonic platforms have also enabled label-free thrombin recognition, illustrating the potential of light–matter coupling to provide additional readout mechanisms for protein detection [189].

Efforts are also directed toward simplifying instrumentation. Gradient quasi-BIC metasurfaces can spatially encode spectral information, enabling spectrometer-free detection through vertical-cavity surface-emitting laser (VCSEL) illumination and complementary metal–oxide–semiconductor (CMOS) imaging [190]. Although validation has primarily involved model proteins, this approach offers a route to low-cost, portable sensing with imaging-based readout.

4.3. Extracellular Vesicles and Viral Particles

4.3.1. Extracellular Vesicles

Extracellular vesicles (EVs) are heterogeneous, complicating quantification and subpopulation analysis. Ultracentrifugation and size-exclusion chromatography support isolation, while nanoparticle tracking characterizes particles; coisolated lipoproteins and protocol differences nevertheless affect purity and quantification. Metasurface assays must address these factors alongside sensitivity and marker specificity [191,192].

Refractometric metasurfaces primarily support EV quantification and surface-marker analysis. Shen et al. integrated gold nanohole arrays with microfluidics and developed a biophysical model based on total EV volume, linking resonance shifts to EV abundance and size distribution to reduce quantification bias caused by size heterogeneity. The platform achieved a detection limit of 141 particles/mL and was evaluated for renal cancer diagnosis and postoperative monitoring in more than 100 samples [193]. This study highlights how quantitative metrics that account for EV heterogeneity can improve the reliability of clinical measurements.

Large-scale studies increasingly combine full-spectrum measurements with data-driven analysis for EV-based disease screening. In 2026, Zhu et al. used the nanoplasmonic metaEVchip to profile glypican-1 (GPC1) and ephrin type-A receptor 2 (EphA2) on serum small extracellular vesicles (sEVs). Full spectra acquired before and after the assay were analyzed using a Kolmogorov–Arnold network (KAN) to classify pancreatic ductal adenocarcinoma (PDAC). As shown in Figure 6d, the platform integrated multidimensional spectral features associated with refractive-index changes and nanoplasmonic loading for combined GPC1/EphA2 analysis. The study included 600 patients with PDAC and 1200 controls, including an independent external validation cohort comprising 120 patients and 240 controls. KAN-based full-spectrum analysis achieved an area under the receiver operating characteristic curve (AUC) of approximately 0.99 in this external validation cohort [194].

Surface functionalization provides additional information on EV subpopulations and disease-associated markers. Plasmonic platforms using epithelial cell adhesion molecule (EpCAM)- and human epidermal growth factor receptor 2 (HER2)-targeting aptamers or combined PSA/CD63 detection have identified EV subpopulations in serum samples from patients with breast or prostate cancer [181,195]. These strategies improve biological specificity, but quantitative results remain strongly dependent on EV isolation protocols, recognition-element immobilization efficiency, and the criteria used to define subpopulations.

SERS can provide broader information on EV molecular composition. Bao et al. developed a cascaded photonic–plasmonic structure that creates a spatially extended "hotspace" capable of encompassing an entire sEV, enabling acquisition of vibrational information associated with both membrane proteins and intravesicular nucleic acids [196].

By addressing the size mismatch between conventional SERS hotspots and EVs, this design extends analysis from vesicle detection to molecular composition.

Complementary platforms address rapid screening and sensitive molecular cargo analysis. Hong et al. combined a Mie-resonant color-changing metasurface with active optofluidic transport to enrich EVs and achieve spectrometer-free colorimetric readout after a 2 min incubation [197]. LSPR-enhanced electrochemiluminescence (ECL) platforms incorporating catalytic hairpin assembly have also been used to detect miRNA-23b-3p in urinary EVs from patients with immunoglobulin A (IgA) nephropathy [198]. These approaches support rapid colorimetric readout and sensitive cargo analysis, respectively, although their clinical validation remains less extensive than that of the refractometric EV platforms discussed above.

4.3.2. Viral Particles

Intact-virus sensing targets particles or their surface antigens without the lysis and amplification used in many nucleic acid assays. Efficient capture, discrimination among viruses, and rejection of nonviral particles remain essential in complex samples [170,199].

Plasmonic platforms operating in the visible and near-infrared regions have relatively extensive experimental support. Ahmed et al. constructed a Fano-resonant metasurface using metallic nanogratings derived from digital versatile discs (DVDs). Protein G enabled oriented immobilization of antibodies against SARS-CoV-2, while integrated microfluidics supported label-free, real-time detection of inactivated intact viral particles. Detectable spectral shifts were observed at low viral concentrations, and the platform distinguished SARS-CoV-2 responses from those associated with influenza viruses and Middle East respiratory syndrome coronavirus (MERS-CoV) [200]. Complementary validation using RT-PCR, ELISA, and scanning electron microscopy (SEM) supported this approach, which combines large-area, low-cost structures with specific biofunctionalization and intact-virus detection.

Sample transport and particle enrichment can also limit intact-virus detection. A 3D-printed hybrid metasurface reported in 2025 integrated superhydrophobic microstructures with nanoplasmonic sensing elements for swine influenza A virus detection. Droplet evaporation and localized plasmonic heating enabled on-chip concentration of a 20 μL sample, with a concentration factor exceeding 4×10^4 estimated from the reduction in droplet volume [201]. This study highlights the value of integrating sample enrichment into metasurface chips to improve the delivery of low-abundance viral particles to the sensing region.

All-dielectric quasi-BIC structures and THz metasurfaces are also being investigated for their potential to approach single-particle sensitivity. High-Q dielectric designs using bacteriophage models have shown promising responses, although the evidence remains primarily numerical [202]. Ji et al. used large-area gold nanogap THz arrays to detect bacteriophage PRD1, exploiting changes in the local dielectric environment when viral particles entered or bridged the nanogaps [203]. Although this approach offers high sensitivity to viral particles, the absence of a specific recognition interface limits discrimination among viral species based on frequency shifts alone. Strategies using chirality or polarization to improve viral discrimination have also been proposed, but remain largely at the simulation stage [204].

4.4. Microorganisms and Cells

For microorganisms and cells, sample delivery is additionally influenced by particle size, sedimentation, adhesion, and shear sensitivity. Their relatively slow diffusion can make capture strongly dependent on channel geometry and flow conditions. Increasing the flow rate may improve replenishment but does not necessarily increase capture probability,

particularly when contact times become too short. Active transport methods, including dielectrophoresis, can improve cell localization near sensing structures. However, capture efficiency, cell viability, and release performance should be evaluated independently of optical sensitivity.

Surface passivation introduces a further trade-off. Polyethylene glycol and zwitterionic coatings can suppress nonspecific adsorption through steric and hydration effects, but their thickness and grafting density also influence receptor accessibility and the separation between targets and enhanced fields. For refractive-index readout, extending the exponential near-field model in Section 2.2.4 to an otherwise unchanged analyte layer displaced outward by a distance (d) gives an overlap-weighting factor of $\exp(-2d/L_d)$, assuming weak perturbation and an approximately unchanged mode profile [86]. The relevant separation depends on the hydrated coating thickness, recognition-layer dimensions, and target-binding geometry. These interfaces should therefore be compared under matched assay conditions in terms of coating thickness, grafting density, nonspecific background, and retained target response. Coating-induced changes in the resonance and near-field profile should also be assessed, particularly when the weak-perturbation approximation is no longer valid. For example, zwitterionic nanoplasmonic bio-meshes functionalized with an L-cysteine monolayer of less than 1 nm thickness achieved a pyocyanin detection limit of 5.6 nM in undiluted human serum [205]. In separate experiments, the platform monitored *Pseudomonas aeruginosa* biofilms in a culture-medium–agar environment over 48 h. This example illustrates thin-interface engineering for antifouling sensing, while serum detection and prolonged biofilm monitoring represent distinct validation conditions.

4.4.1. Bacterial Detection and Clinical Infection Diagnostics

Metasurface bacterial sensing follows two routes: classification of intact bacteria from dielectric or spectral fingerprints, and targeted capture from clinical samples. Both require low-load sensitivity and species discrimination, while the need for prior culture and compatibility with clinical matrices determine their practical utility [206,207].

The fingerprinting route exploits differences in dielectric properties and full-spectrum responses among microbial species. Zhong et al. reported species-dependent concentration–frequency-shift responses for two *Staphylococcus* species using a THz metasurface [208]. Yu et al. combined the full transmission spectra of an all-dielectric metagrating with machine learning to classify eight clinical pathogens. The best-performing model achieved 97.5% accuracy, while external validation accuracy exceeded 96% in two independent cohorts of clinical isolates [209]. This approach avoids the need to develop a separate antibody recognition interface for each target. However, the samples primarily comprised cultured clinical isolates, making this a method for rapid identification after culture rather than direct testing of patient specimens.

Microfluidic integration can further improve automated sample transport and measurement consistency. THz chips incorporating microfluidics have been used to quantify and distinguish microorganisms including *Candida albicans*, *Staphylococcus aureus*, and *Escherichia coli* [210]. Multiparameter THz readout can further lower detection thresholds, although greater sensitivity alone does not ensure species specificity.

Surface functionalization is increasingly important for clinical detection. Ma et al. combined a quasi-BIC metal–graphene THz metasurface with a boronic acid-functionalized capture interface, nanoparticle enhancement, and microfluidics. The platform achieved detection limits of 11–14 colony-forming units (CFU) mL^{-1} for *E. coli*, *S. aureus*, and *Pseudomonas aeruginosa* and underwent preliminary evaluation using samples from 10 patients with suspected bacteremia. Positive results were obtained approximately 5 h earlier, on average, than with conventional blood culture. The platform also enabled bacterial inac-

tivation through combined photothermal effects and reactive oxygen species [211]. This work demonstrates the integration of capture, detection, and inactivation, although its clinical validation remains limited by the small sample size.

More direct evidence from clinical specimens comes from the Plasmonic Array Nanohole Technology on Metal–Insulator–Metal (PANTOMIM) platform. As shown in Figure 6e, Kurt et al. developed an Au/SiN/Al MIM nanohole array whose waveguide architecture suppresses metal–substrate-associated resonances, improving the extinction and spectral purity of the target resonance under aqueous sensing conditions. Antibody functionalization enabled specific capture of uropathogenic *E. coli* (UPEC). Following simple sample filtration, detection was completed in approximately 15 min. In a clinical cohort comprising 50 UPEC-positive and 50 UPEC-negative urine samples, the platform achieved an accuracy above 90% and an AUC of 0.972 [212]. By reducing reliance on bacterial culture before analysis, this approach demonstrates the potential of combining specific surface recognition with high-extinction, spectrally selective readout for clinical point-of-care testing. Its current focus on UPEC nevertheless requires further validation in larger cohorts and extension to multiple pathogens.

4.4.2. Live-Cell Sensing and Functional Monitoring

Live-cell sensing monitors adhesion, barrier integrity, phenotypes, molecular composition, and drug responses. Continuous readout must preserve viability and minimize measurement-induced perturbations [213,214].

Visible-light MetaSPR platforms convert changes in cell coverage and the cell–chip interface into continuously measurable optical responses. As shown in Figure 6f, Chen et al. developed a MetaSPR colorimetric cell chip (MetaSPRCS) to track Caco-2 cell adhesion, proliferation, and barrier formation, followed by ethanol-induced barrier damage and dihydroquercetin (DHQ)-mediated repair kinetics [215]. Related MetaSPR nanocup arrays have been incorporated into metasurface plasmon resonance microscopy (Meta-SPRM) and 96-well plate platforms for cell adhesion imaging, drug screening, and monitoring of immune-cell-mediated killing [216,217]. These studies highlight the value of metasurfaces for label-free, continuous monitoring of cellular function over extended periods, with opportunities for high-throughput analysis.

THz metasurfaces primarily distinguish cellular phenotypes or states through changes in overall dielectric properties. Liu et al. developed a bilayer THz metasurface with rotationally misaligned resonators on opposite sides of a dielectric spacer. The platform combined high-Q resonance sensing with machine learning to assess MCF-7 cell concentrations and the proportions of viable, apoptotic, and necrotic cells following paclitaxel treatment [218]. Other quasi-BIC and nanostructured metasurfaces have been explored for monitoring macrophage polarization, oxidative-stress-induced apoptosis, and tumor or neuronal cell states [219–221]. These methods require no fluorescent labeling, but their readouts primarily reflect overall dielectric responses. Specific discrimination among phenotypically similar subpopulations and generalizability across cell types therefore remain important challenges.

Enhanced mid-infrared spectroscopy provides complementary information on intracellular molecular composition. Mahalanabish et al. used a three-dimensional metal–dielectric metasurface to extend enhanced near fields into cells and investigate endocytosis through changes in vibrational bands, including amide I [222]. Kelp et al. combined electrically biased plasmonic metasurfaces with microfluidic channels to capture live cells by dielectrophoresis and acquire their infrared spectra in real time from flowing suspensions [223]. These approaches extend cellular analysis beyond enumeration by combining molecular spectroscopy with controlled interactions between cells and sensing surfaces.

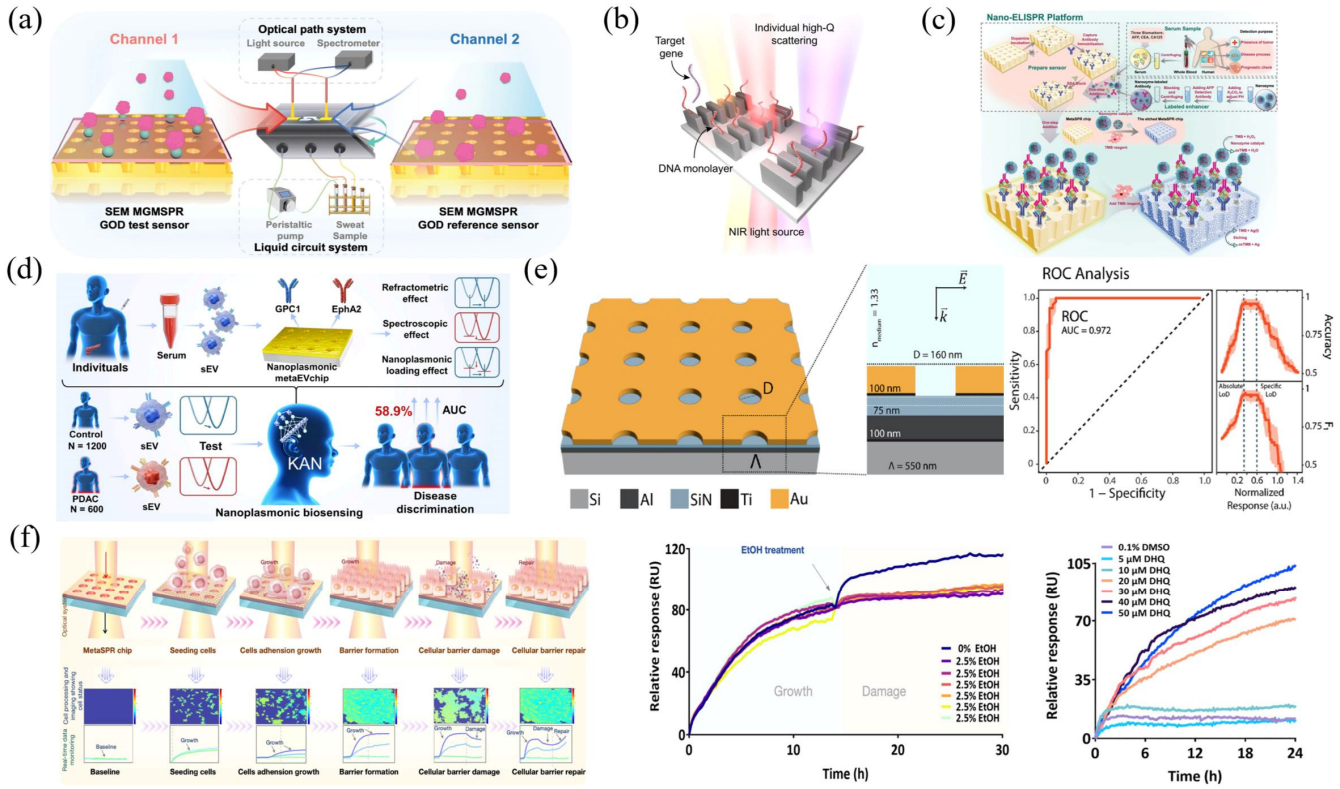


Figure 6. Representative metasurface-enhanced biosensing platforms from molecules to cells. (**a**) MXene–graphene oxide MetaSPR sensor for continuous glucose monitoring in artificial sweat (adapted from [164], 2025). (**b**) High-Q silicon metasurface for SARS-CoV-2 gene-fragment detection (adapted from [172], 2023). (**c**) Nanozyme-enhanced MetaSPR immunoassay for cancer biomarkers (adapted from [180], 2023). (**d**) Nanoplasmonic metaEVchip for PDAC classification based on GPC1/EphA2 signatures (adapted from [194], 2026). (**e**) Au/SiN/Al nanohole array for direct detection of uropathogenic *E. coli* (adapted from [212], 2025). (**f**) MetaSPR cell chip for real-time monitoring of Caco-2 barrier damage and recovery (adapted from [215], 2026).

A dual-mode mid-infrared plasmonic metasurface simultaneously measured amide I/II vibrational fingerprints and resonance shifts in a spectrally silent region for real-time monitoring of drug responses in living human cancer cells [224], linking molecular fingerprints with changes in cellular mass or dielectric properties.

For cell analysis in biofluids, Wang et al. integrated a sloped microchannel with a THz metasurface to quantify leukocyte concentrations and polymorphonuclear-to-mononuclear cell ratios in clinical cerebrospinal fluid (CSF) samples from post-craniotomy patients with suspected central nervous system infection [225]. A tetrahedral-DNA/anti-EpCAM-functionalized THz microfluidic platform also enabled specific capture and detection of viable A549 tumor cells [226].

4.5. Summary

Across molecular, particle, and cellular targets, biosensing requirements expand from molecular specificity and weak-signal resolution to efficient capture, matrix tolerance, subpopulation discrimination, and functional monitoring. Table 3 summarizes representative performance and validation across these scales.

Table 3. Representative biosensing strategies, validation status, and key limitations.

Application	Main Strategies	Representative Results	Validation Status	Key Limitations
Small molecules	MetaSPR assays; SERS fingerprinting; THz sensing	Hormone/vitamin assays [162,163]; drug/metabolite and continuous glucose/nicotine monitoring [164,168,169]	Whole blood and serum [162,163,168]; artificial sweat and wearable monitoring [164,169]; THz model systems [166,167]	Weak interfacial responses; matrix interference; recognition stability; batch reproducibility
Nucleic acids	High-Q hybridization; molecular amplification; enhanced fluorescence/THz readout	Direct-hybridization LOD: 8 fM in buffer [172]; HCR/nanoparticle-assisted ctDNA LOD: 0.22 fM [175]	Buffers and spiked swab eluates [172]; plasma from 12 patients and 12 controls [175]; other small clinical studies [173,174]	Sensitivity; mismatch discrimination; multiplexing; contamination
Protein biomarkers	MetaSPR immunoassays; nanozyme amplification; SERS/quasi-BIC sensing	AFP, CEA, and CA125 quantification [180]; multiplexed sepsis-marker detection [185]	60 serum samples [180]; 80 plasma samples [185]	Functionalization reproducibility; nonspecific adsorption; calibration drift
Extracellular vesicles	Nanohole sensing; selective capture; spectral/KAN analysis; SERS/ECL	LOD: 141 particles/mL [193]; external-validation PDAC AUC: ≈ 0.99 [194]	Renal-cancer study: >100 samples [193]; PDAC cohort: 1800 participants, including 360 in external validation [194]	EV heterogeneity; normalization; cross-center generalizability
Viral particles	Fano resonances; on-chip enrichment; quasi-BIC/THz sensing	SARS-CoV-2 detection [200]; estimated volume-based enrichment factor: $>4 \times 10^4$ [201]; low-count PRD1 detection [203]	Laboratory virus studies [200,201,203]; numerical proposals [202,204]	Capture efficiency; virus discrimination; biosafety; multiplexing
Bacteria	THz/machine learning fingerprinting; quasi-BIC sensing; PANTOMIM	Isolate-classification accuracy: 97.5% [209]; LOD: 11–14 CFU/mL [211]; urine-sample AUC: 0.972 [212]	Cultured clinical isolates [209]; 10 suspected-bacteremia cases [211]; 50 UPEC-positive and 50 UPEC-negative urine samples [212]	Culture dependence; low-load detection; species identification
Living cells	MetaSPR imaging; quasi-BIC/THz sensing; infrared fingerprinting; microfluidics	Caco-2 barrier dynamics [215]; MCF-7 cell-state analysis [218]; live-cell drug responses [224]; clinical CSF leukocyte analysis [225]	Cell-culture models and live-cell assays [215–224]; clinical CSF specimens [225]	Culture compatibility; photothermal effects; phenotypic specificity

Selected protein, EV, and bacterial platforms have been tested in cohorts ranging from tens to more than a thousand samples. Diagnostic AUCs should be accompanied by cohort composition, confidence intervals where available, and sensitivity and specificity at a defined threshold; agreement with quantitative reference assays is a separate question. Remaining barriers include amplification dependence, variability in functionalization and sample processing, limited multicenter validation, and challenges in portable system integration. Future evaluation should integrate sample processing, interfacial recognition, sensor readout, algorithm validation, and comparison with established clinical reference methods.

5. Metasurface-Enhanced Environmental Monitoring

Environmental sensing must distinguish target responses from changing temperature, humidity, matrix composition, and surface fouling [32,227,228]. Air, water, and soil applications are considered separately, with emphasis on real-sample validation, quantitative reliability, and sustained operation.

5.1. Atmospheric Monitoring

5.1.1. Combustible and Greenhouse Gases

Pd-based H_2 sensors exploit changes in dielectric properties upon hydrogen uptake, whereas CO_2 platforms use molecular absorption or adsorption-mediated responses. Practical operation also depends on response time, drift, and tolerance to water vapor and temperature changes.

As shown in Figure 7a, Nugroho et al. used particle swarm optimization to jointly optimize the diameter and height of Pd nanodisks, the array period, and the thickness of a poly(methyl methacrylate) (PMMA) overlayer. The optimization used an application-specific FOM defined as the hydrogenation-induced peak shift divided by the resonance linewidth, which differs from the bulk refractive-index FOM in Equation (5). LSPR enhanced hydrogenation-induced peak shifts, while surface lattice resonances narrowed the spectral linewidth [229]. The optimized periodic array produced resolvable, stepwise peak shifts over 0.25–1000 ppm H_2 at room temperature with Ar as the carrier gas. The lowest experimentally tested concentration was 250 ppb. An LOD of approximately 200 ppb was estimated by extrapolating the concentration response to a peak-shift threshold of 3σ, where the reported signal noise was $\sigma \approx 0.01$ nm, corresponding to a threshold of approximately 0.03 nm [229]. At 250 ppb, the response time was approximately 40 min in Ar with the thick PMMA overlayer. Separately, a tandem coating comprising 295 nm PMMA and 5 nm poly(vinyl alcohol) (PVOH) enabled detection down to 250 ppb in synthetic air by restricting oxygen access to the Pd surface [229]. Faster response and recovery, together with validation under variable humidity and temperature, remain necessary for practical deployment. Fiber-integrated optical readout has also been explored in Pd-based hydrogen sensors, providing a potential route toward compact and remote sensing configurations [230].

Much of the CO_2 metasurface research reviewed here focuses on high-Q resonator design and adsorption-assisted refractive-index sensing. For example, PHMB-functionalized quasi-BIC THz metasurfaces translate CO_2 adsorption into predicted frequency shifts, with performance derived mainly from modeling and numerical simulations [120]. Atmospheric CO_2 monitoring requires resolution of small fluctuations around background concentrations of several hundred ppm, together with robustness against water-vapor absorption, temperature changes, and coexisting gases. Many of these platforms therefore remain at the proof-of-concept stage, with continuous operation under realistic atmospheric conditions requiring further validation.

5.1.2. Toxic Gases and Volatile Organic Compounds

Overlapping molecular bands, water vapor, and broad concentration ranges complicate toxic-gas and VOC discrimination. Multichannel spectroscopy, selective adsorption, and data-driven analysis offer complementary routes to improved selectivity.

Multichannel infrared platforms have progressed to experimental validation. Tan et al. directly integrated $Au/SiO_2/Au$ narrowband absorbers into a pyroelectric detector array, providing eight spectral channels covering characteristic bands of H_2S, CH_4, CO_2, CO, NO, CH_2O, NO_2, and SO_2. The system also enabled concentration retrieval from binary CO/SO_2 mixtures [231]. Distinct spectral weighting across channels can help mitigate

interference from overlapping absorption bands. However, the experiments used standard cylinder gases mixed with N_2, which do not fully represent ambient air containing water vapor, particulates, and other background constituents.

The compact infrared module in Section 3.1.2 occupies approximately 1 cm^3, weighs approximately 1 g, and achieved 98.4% overall accuracy in an independently acquired test conducted two days later, using one target gas at a time [136]. The PVP-functionalized THz platform in Section 3.1.1 demonstrated trace-VOC detection under controlled room-temperature conditions [131]. Both still need validation with multicomponent mixtures, across temperature and humidity variations, and over extended operation.

Functional materials can also simplify gas-warning readout. For example, liquid crystals integrated with metasurface holography can convert VOC-induced changes in liquid-crystal orientation or optical state into visible patterns [232]. This visual format avoids complex spectral analysis, but reliable discrimination among VOCs and stable operation under changing temperature and humidity remain challenging.

5.1.3. Water Vapor and Aerosol Particles

Water vapor is both a sensing target and a major interference source. In terahertz measurements, gas-phase water absorption can overlap with useful spectral features, while adsorbed water can change the dielectric response, swelling, and sorption equilibria of functional layers. Temperature fluctuations can additionally alter resonator dimensions, material optical constants, adsorption kinetics, and source or detector output. These effects can produce resonance shifts or intensity changes that resemble analyte responses. Consequently, temperature and relative humidity should be varied independently during calibration and subsequently tested in combination. Blank reference channels, simultaneous environmental measurements, and validation of compensation models under conditions excluded from training are needed to establish whether the target response remains distinguishable from background drift [32,130,136,233].

Liu et al. integrated a Au metasurface and a humidity-sensitive GO layer onto the end face of a multimode optical fiber. Dynamic time warping was used to compare full reflection spectra with a calibration database spanning 20–90% relative humidity (RH). Reversibility and repeatability were further evaluated over seven humidity cycles between 15% and 80% RH [233]. Full-spectrum similarity analysis uses more response information than single-peak tracking. However, validation has primarily involved controlled laboratory humidity conditions; long-term baseline stability under outdoor temperature variations, pollutant deposition, and exposure to multiple gases remains insufficiently characterized.

Aerosol detection introduces additional challenges associated with particle transport, deposition, and size distribution. In 2026, Xing et al. integrated an aerosol transport system with a THz metasurface supporting Friedrich–Wintgen quasi-BICs and demonstrated detection of artificially generated SARS-CoV-2 spike-protein aerosols under simulated exhalation conditions [234]. These results support the feasibility of combining high-Q resonances with aerosol enrichment and transport. However, the experiments were limited to prepared protein aerosols; performance with patient breath, naturally occurring bioaerosols, and ambient particulate matter remains to be established.

5.2. Water Quality Monitoring

5.2.1. Heavy Metal Ions

Trace metal ions produce small bulk refractive-index changes that can be obscured by abundant background ions. Concentration-dependent dielectric responses alone therefore do not demonstrate metal-ion selectivity.

Changes in ionic strength modify the interfacial electrical double layer and electrostatic screening, which can alter ion partitioning, aptamer conformation, and nonspecific adsorption at a functionalized surface. These changes can influence an optical signal indirectly through binding and local composition, in addition to the bulk refractive-index contribution. The electrical screening length should not be equated with the optical near-field decay length. Selective metal-ion sensing therefore requires calibration at controlled pH and ionic strength, followed by interference tests involving realistic concentrations of major background ions and natural organic matter [36,235].

Almawgani et al. simulated the responses of a patterned graphene metasurface to Cu^{2+} and Mg^{2+} solution models assigned different refractive indices, reporting a sensitivity of 113.92 GHz/RIU [235]. These simulations demonstrate sensitivity to differences in dielectric environment, but rely entirely on prescribed refractive-index values, without device fabrication, competing-ion tests, or analysis of real water samples. The reported sensitivity therefore characterizes a refractometric response and does not establish Cu^{2+}-specific recognition.

A transferable strategy for selective ion recognition is provided by the Cd^{2+} aptamer platform of Shen et al., in which target-induced conformational changes modulate coupling between Au nanoparticles and a plasmonic metasurface [36]. The authors reported an LOD of approximately 3.72 pg/L in ultrapure water and evaluated complex-matrix performance primarily in biofluids. These results demonstrate selective interfacial transduction but do not establish performance in environmental waters. Application to river water, lake water, or industrial wastewater requires validation against variations in pH, hardness, natural organic matter, and competing metal ions.

5.2.2. Organic Pollutants and Biotoxins

SERS fingerprints and recognition-functionalized resonators offer complementary routes to detecting dilute organic pollutants and biotoxins in water, where bulk refractive-index changes provide limited chemical selectivity.

Natural organic matter, including humic substances, can introduce broad fluorescence backgrounds in Raman measurements, compete with target molecules for adsorption sites, and block access to hotspots. Suspended particles can add scattering and promote nonuniform deposition, while dissolved organic components may contribute overlapping spectral bands. Baseline correction can reduce broad spectral backgrounds but cannot recover analytes excluded from sensing sites by competitive adsorption. Matrix-matched calibration, recovery measurements at multiple concentrations, and comparison of filtered and unfiltered samples are therefore needed to determine whether sample treatment improves optical readout at the expense of analyte recovery [236,237].

Li et al. functionalized Ag nanocubes with different molecules so that pesticide binding altered interparticle spacing and generated additional SERS hotspots. Combined with deep learning, the platform distinguished six organophosphorus pesticides [236]. Spiking experiments using water samples collected from farmland, rivers, and fishponds yielded recoveries of 86.4–115.4% and relative standard deviations (RSDs) of 2.84–6.21% at concentrations of 5–80 μg/L. The workflow from sampling to result interpretation took approximately 30 min. These recovery, precision, and analysis-time data provide a practical basis for assessing environmental applicability beyond enhancement factors measured in standard solutions. However, the lowest spiking concentration should not be interpreted as a formal LOD, and further validation using unspiked environmental samples and blinded testing remains necessary.

SERS structures with dense nanogaps also support trace organic-dye detection. For example, a hybrid structure combining flow-through nanopores with Ag nanoparticles

detected malachite green at sub-ppb concentrations in standard aqueous solutions [237]. This performance remains to be validated in environmental waters containing natural organic matter and suspended solids.

For toxins with established biorecognition elements, high-Q metasurfaces can combine sensitive optical readout with chemical selectivity. Ma et al. coupled a silicon-disk quasi-BIC metasurface with antigen–antibody recognition to detect microcystin-LR (MC-LR) at low concentrations [238]. The high-Q structure improves the resolvability of weak binding-induced spectral changes, while selectivity primarily derives from the biorecognition interface. Suppression of nonspecific adsorption, antibody stability, and effective regeneration of the sensing surface are therefore important for practical operation in complex water samples.

5.2.3. Microplastics and Drinking Water Quality Anomalies

Plastic-particle measurements must account for size-dependent responses, limited refractive-index contrast, and interference from suspended solids and biological debris. Particle capture, size-distribution analysis, and imaging therefore complement enhanced optical readout.

In 2025, Ece et al. introduced MicroMetaSense, which combines dye labeling with fluorescence enhancement by plasmonic near fields. The minimum detectable masses of PMMA and poly(ethylene terephthalate) (PET) in spiked aqueous samples were 183 and 205 fg, respectively. The platform was further evaluated using real tap-water and lake-water samples, as well as artificial seawater [239]. Measurements covered particle sizes of approximately 250 nm–100 μm, with an analysis time below 30 min, supporting a relatively low-cost approach to sensitive particle detection in complex aqueous matrices. However, the platform demonstrates sensitive plastic-particle detection but does not establish polymer-type classification based on the metasurface response.

For broader water-quality assessment, Sperling et al. arranged eight Au metasurfaces with different surface chemistries in series within a microfluidic channel, as shown in Figure 7b. Differential resonance shifts across these partially selective surfaces generated a water-quality fingerprint [240]. Linear discriminant analysis was used to distinguish influent (INF) and treated effluent (EFF) samples collected from drinking water treatment works. Fivefold cross-validation with 25 repeated training–validation selections yielded a mean validation accuracy of 81.8%. Three tap water samples collected at the point of use and not included in training all produced response patterns more similar to INF within the model. This approach uses collective response patterns to screen for water-quality differences without requiring a dedicated recognition element for each contaminant. However, samples underwent freezing, thawing, and filtration before measurement, and continuous operation at a water treatment facility has not been demonstrated. The study therefore represents a laboratory proof of concept using real water samples.

5.3. Soil and Agricultural Monitoring

Soil dielectric responses depend jointly on moisture, salinity, clay content, and organic matter. Current approaches use extraction or other pretreatment for contaminant analysis, or multifrequency and multimode sensing of bulk properties. Soil heterogeneity and preparation-induced matrix changes limit reproducibility and transfer across soil types and regions [241–243].

5.3.1. Pesticide Residues

Pesticide sensing in soil and agricultural products is constrained by uneven residues and matrix interference. THz measurements often require pretreatment to reduce water absorption; SERS requires reproducible hotspots and efficient analyte enrichment or delivery.

Some THz metasurface studies have explored pesticide sensing numerically, including calculations of mass and refractive-index responses for multiple pesticides in model wheat-flour matrices [241]. These studies support structural design and assessment of potential analyte responses. However, without device fabrication and experiments using real samples, their predictions do not establish detection limits under environmental conditions.

SERS metasurfaces have progressed to testing in agricultural extracts. In 2026, Vural Kaymaz et al. combined a hexagonal Au MIM SERS metasurface with deep learning to distinguish six pesticides and conducted experiments using cucumber extracts [242]. By integrating dense hotspots with data-driven classification, this study extended evaluation from standard molecular spectra to complex agricultural matrices. Nevertheless, sample extraction remained necessary, and continuous in situ field monitoring was not demonstrated.

Related SERS nanostructures have also been applied to soil analysis. A system based on coupled graphene-coated Ag nanoparticles enabled quantitative detection of thiram in spiked soil [244], supporting the applicability of SERS to solid agricultural matrices. However, the effects of soil type, moisture content, and humic substances have yet to be systematically compared. Transferable Au@Ag SERS substrates have also enabled direct collection of pesticide residues from strawberry, apple, and mushroom surfaces [245], offering a route to simpler on-site sampling with reduced sample transfer.

In soil extracts, humic fluorescence and competitive adsorption should additionally be evaluated together with extraction recovery, because improved spectral clarity after pretreatment does not necessarily indicate unbiased recovery of the original soil contaminant.

5.3.2. Soil Moisture and Nutrients

Moisture and nutrient estimates from soil dielectric responses can be confounded by temperature, salinity, clay, density, and organic matter. Multifrequency measurements and calibration across soil types are needed to separate these contributions.

Extending metasurface concepts to microwave frequencies, Amiri et al. demonstrated a passive absorber based on substrate-integrated waveguide cavities, with moisture-dependent responses across multiple resonance bands [243]. Experimental validation used sandy soil under controlled laboratory conditions. Further assessment should address interference from other soil properties and verify performance across soil types using independent samples.

In 2026, Wang et al. introduced SoilNutri, a passive, battery-free underground sensing capsule based on a complementary split-ring metasurface, as shown in Figure 7c. The system uses ground-based or drone-mounted ultra-wideband (UWB) radar to acquire reflected signals and a data model to jointly estimate soil moisture and nitrogen content [246]. Model performance was evaluated using root-mean-square error (RMSE) and mean absolute error (MAE); the reported MAEs were approximately 0.64% for moisture and 5.14 ppm for nitrogen content, while the material cost per sensing unit was below US$1. The integration of passive wireless readout, simultaneous estimation of two parameters, and field validation under the reported test conditions demonstrates a promising route toward large-scale agricultural deployment. Nevertheless, the reported experiments were conducted at a relatively stable ambient temperature of approximately 15 °C [246], leaving robustness across broader temperature variations to be established. Encapsulation aging during prolonged burial, changes in soil compaction, biological activity, and regional variations in mineral composition may also affect model transferability. Further development requires sustained testing across multiple sites, seasons, and temperature conditions, supported by representative reference soils and calibration databases.

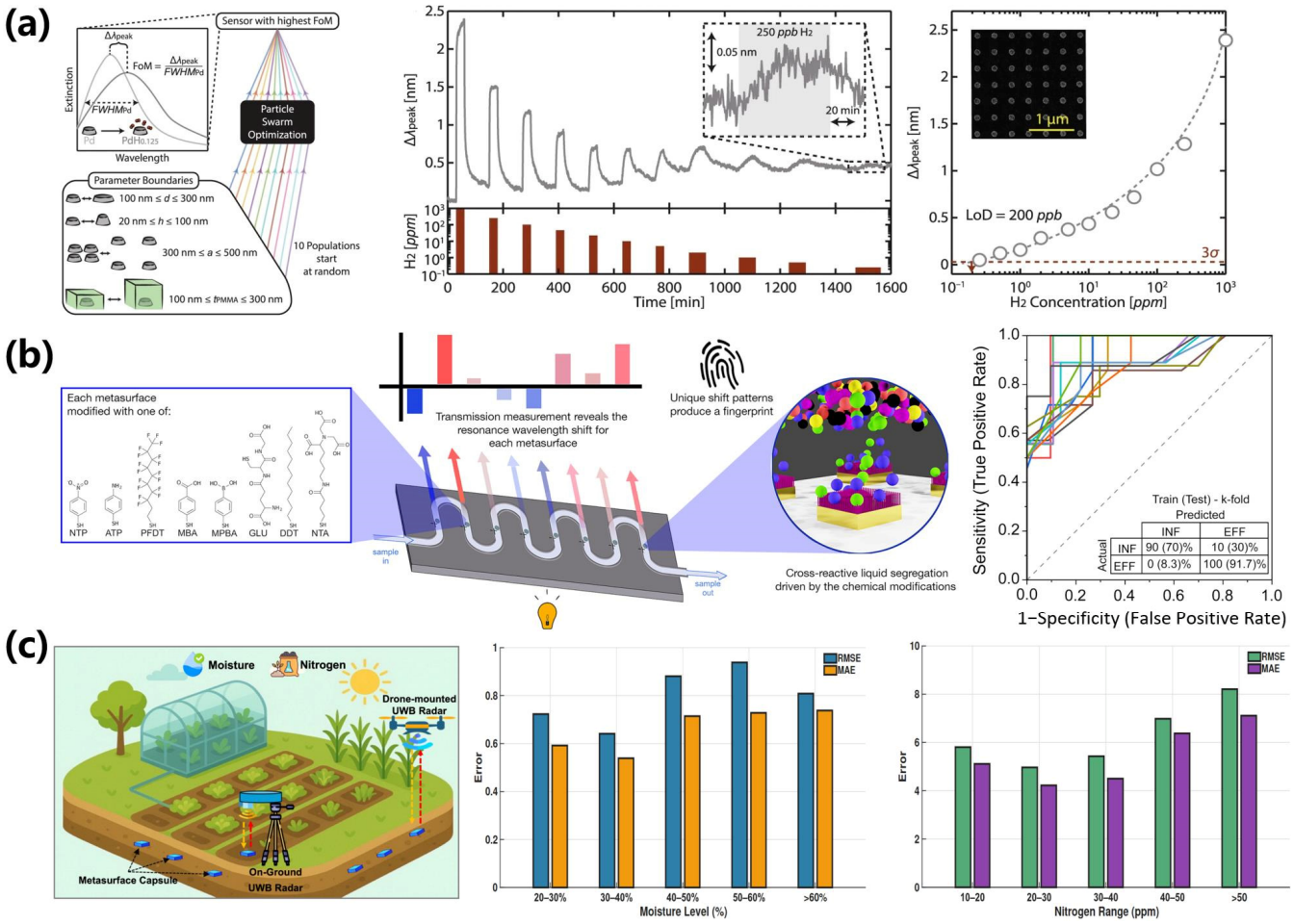


Figure 7. Representative metasurface-enabled platforms for environmental monitoring. (**a**) Pd nanodisk arrays for hydrogen sensing (adapted from [229], 2022). (**b**) Cross-reactive nano-tastebud array for water-quality classification (adapted from [240], 2023). (**c**) Passive SoilNutri capsules for soil moisture and nitrogen sensing (adapted from [246], 2026).

5.3.3. Mycotoxins in Agricultural Products

Mycotoxin detection is included as a complementary agricultural application, primarily validated in food and feed extracts. Low target concentrations and complex matrices motivate selective antibody or aptamer interfaces, with performance assessed through real-sample validation, stability, and comparison with reference methods.

As a related enhanced spectroscopic platform, Chen et al. developed a competitive immunoassay for AFB_1 using photonic crystal microspheres and SERS nanotags in 2026. The assay yielded a calculated LOD of 0.988 pg/mL and a reported linear dynamic range of 1 pg/mL–100 ng/mL. After storage at 4 °C for 14 days, the sensor retained approximately 89.2% of its initial SERS signal. Performance was further evaluated using spiked corn and oat samples and compared with ELISA [247]. These data extend performance evaluation beyond detection limits to complex-matrix compatibility and storage stability. However, the incubation and washing steps required by the competitive immunoassay add to workflow complexity.

Veliz et al. integrated aptamer-functionalized Au nanoholes with flow-through microfluidics for AFB_1 detection in maize, coffee, and rice extracts [248]. The workflow included a 10 min flow-assisted incubation at 5 µL/min before SERS acquisition. Controlled sample transport and testing in food extracts support the platform's relevance to

agricultural screening. Sample extraction remains necessary, and direct in situ detection during field use, storage, or transport has yet to be demonstrated.

5.4. Summary

Across atmospheric, water, and soil monitoring, sensing strategies increasingly combine selective interfaces, multichannel readout, and data-driven analysis rather than relying on single-resonance responses alone. Table 4 compares representative strategies, results, validation conditions, and deployment limitations.

Table 4. Representative environmental sensing strategies, validation status, and key limitations.

Application	Main Strategies	Representative Results	Validation Status	Key Limitations
Atmosphere	Pd hydrogenation; multichannel infrared spectroscopy; THz enrichment/readout	H_2 tested down to 250 ppb; extrapolated LOD: ≈200 ppb [229]; overall classification accuracy: 98.4% in single-target-gas tests [136]; reported VOC LODs: 8.2–12.2 ppb [131]	Controlled gas tests [131,136,229,231]; laboratory humidity and protein-aerosol studies [233,234]	Slow low-concentration response; temperature/humidity interference; mixture discrimination; drift
Water	Recognition interfaces; SERS/machine learning; quasi-BIC sensing; fluorescence; cross-reactive arrays	PMMA/PET minimum detectable masses: 183/205 fg [239]; cross-validated water classification: 81.8% [240]	Environmental-water spiking [236]; tap/lake water and artificial seawater [239]; treatment-water and tap-water analysis [240]	Matrix interference; fouling; regeneration; model transferability
Soil and agriculture	SERS; direct surface sampling; passive metasurfaces; data-driven sensing	SoilNutri MAEs: ≈0.64% moisture and ≈5.14 ppm nitrogen [246]; AFB_1 LOD: 0.988 pg/mL [247]	Extracts or spiked samples [242,244,247,248]; laboratory soil tests [243]; field soil sensing [246]	Soil heterogeneity; moisture/salinity coupling; regional calibration; encapsulation aging

Validation remains uneven: atmospheric studies mainly use prepared gas mixtures or artificial aerosols, water studies increasingly use real samples in offline laboratory measurements, and soil-pollutant studies commonly rely on extracts or spiked samples. Some passive soil-sensing platforms provide field evidence.

6. Conclusions and Outlook

Metasurface sensing increasingly combines resonant enhancement with selective interfaces, sample handling, and multidimensional readout. Across the reviewed applications, high Q factors, strong field enhancement, and low detection limits alone do not establish reliable performance in complex samples.

Table 5 retains the original modeling, measurement, and validation contexts. Its metrics are not interchangeable and should not be combined into a single ranking. Tested concentration intervals must be distinguished from validated quantitative ranges, and calculated or extrapolated LODs from the lowest experimentally tested concentrations.

Overall, sensing performance is set by the entire measurement chain: the resonator determines the accessible field distribution and spectral response; sample transport determines how much analyte reaches that field; recognition chemistry governs selective capture or interaction; the matrix introduces competing adsorption and background signals or fluc-

tuations; and the readout converts these interactions into a calibrated estimate. Improving one component may expose a limitation elsewhere. A narrower resonance, for example, provides little analytical benefit if binding is transport-limited or environmental drift exceeds the analyte-induced shift. Evaluation should therefore combine optical metrics with repeatability, fabrication reproducibility, matrix compatibility, and operational stability.

Table 5. Selected quantitative performance measures and their validation context.

Study/Platform	Evidence/Test Conditions	Selected Reported Metrics	Interpretation/Validation Context
A. Optical and modeled sensing metrics			
PHMB-coated THz CO_2 sensor [120]	Numerical	Concentration sensitivity: 0.06 GHz/ppm; theoretical LOD: ≈33.3 ppm	Depends on the functional-layer model; requires experimental gas-exposure calibration
Six-band AlCuFe absorber [98]	Numerical	Maximum sensitivity: 3000 GHz/RIU; maximum Q: 165.34; maximum FOM: 56.82 RIU^{-1}	Reported maxima may correspond to different resonances or parameter conditions and should not be interpreted as a single operating point
Four-band AlCuFe absorber [100]	Numerical	Maximum reported sensitivity: 3120 GHz/RIU; maximum Q: 108.08; maximum FOM: 28.65 RIU^{-1}	Maxima may correspond to different resonances/settings; no analyte-specific or practical analytical validation
Five-band graphene absorber [109]	Numerical	Wavelength sensitivities: 930.6–1134.3 nm/RIU	Calculated responses to changes in ambient refractive index; no analyte-specific LOD can be inferred
B. Analytical measurements, validation, and workflow-dependent performance			
Mid-infrared gas-classification platform [136]	CO_2/CH_4: 10–100%; NH_3: 100–1000 ppm; MEK: 200–400 ppm	Overall hold-out accuracy: 98.4%; class-specific true-positive rates: 94.4–100%	An independent dataset was acquired two days later; this supports short-term transferability but does not establish long-term field stability
Ag-pSi mycotoxin SERS platform [143]	Concentration calibration; separate spike-recovery tests in wheat, maize, and rice	Calculated LODs: 0.008, 0.547, and 0.922 ppb for AFB_1, FB_1, and OTA, respectively	Food-sample recoveries: 95–104%; RSDs: 1.5–6.6%. These assess sample-workflow performance, separately from calibration-based LODs
Silicon DNA metasurface [172]	Physiological buffer; separately tested spiked nasopharyngeal swab eluates	Average Q: ≈2200; LOD: ≈8 fM in buffer	Response within ≈5 min at 100 nM in spiked swab eluates; the swab-response condition is different from that used to determine the buffer LOD
HCR/nanoparticle-assisted ctDNA sensing [175]	Analytical calibration; separate plasma evaluation involving 12 patients and 12 healthy controls	Reported assay LOD: 0.22 fM	Includes HCR and nanoparticle-mediated amplification; small-cohort plasma evaluation should be distinguished from analytical LOD determination
Ag/MOF fiber SPR sensor [165]	Glucose calibration range: 0.1–1.2 mg/mL	Wavelength sensitivity: 9.99 nm/(mg/mL)	Enzyme-functionalized experimental platform; the reported calibration response should not be interpreted as evidence of clinical diagnostic performance
Pd hydrogen sensor [229]	0.25–1000 ppm H_2 in Ar; additional synthetic-air tests	Ar: lowest tested concentration, 250 ppb; extrapolated LOD, ≈200 ppb. Synthetic air: detection demonstrated at 250 ppb	Response time: ≈40 min at 250 ppb in Ar, illustrating a sensitivity–kinetics trade-off

Table 5. *Cont.*

Study/Platform	Evidence/Test Conditions	Selected Reported Metrics	Interpretation/Validation Context
Environmental-water SERS platform [236]	Water samples spiked at 5–80 μg/L	Recoveries: 86.4–115.4%; RSDs: 2.84–6.21%	Total workflow: ≈30 min; the lowest spike level should not be treated as a formally established LOD
Photonic-crystal/SERS AFB_1 assay [247]	AFB_1 calibration solutions; separate spike-recovery tests in corn and oat samples	Calculated LOD: 0.988 pg/mL; reported linear dynamic range: 1 pg/mL–100 ng/mL	≈89.2% signal retained after 14 days at 4 °C; this represents storage stability rather than continuous operational drift

The photonic-crystal/SERS AFB_1 assay reported intra- and interassay coefficients of variation of 7.45% and 6.73%, respectively, at 10 ng/mL [247]. The Ag-pSi aptasensor maintained comparable responses through four regeneration cycles and, separately, during three weeks of storage at 4 °C [143]. These measurements assess assay precision, regeneration, and storage stability; they do not establish reproducibility across independently fabricated batches or quantify continuous baseline drift.

6.1. Data Processing and Machine-Learning Validation

Machine learning can assist spectral classification, concentration estimation, and inverse design, but the validation strategy must match the intended use. Preprocessing should document baseline correction, denoising, wavelength alignment, normalization, and treatment of missing or saturated channels. Any preprocessing parameters, feature selection, or dimensionality reduction learned from data must be fitted within the training partition. Applying these steps to the complete dataset before splitting can leak information from the test set and produce optimistic performance estimates.

Physically defined features, such as resonance positions, linewidths, intensity ratios, and integrated band areas, provide interpretable inputs. Data-driven alternatives include principal component analysis for dimensionality reduction and recursive feature elimination for selecting wavelength subsets. These representations should be compared with full-spectrum models using identical patient- or site-level data partitions. Feature selection and model tuning should be restricted to the inner training folds of a nested validation procedure, with selection stability examined across folds.

Data partitions should preserve the independence of the underlying specimens. Repeated spectra, aliquots, or measurements from one patient should remain in the same partition; environmental datasets may additionally require grouping by collection site, sampling period, device, or fabrication batch. Model selection should use an internal validation procedure, followed by evaluation on an untouched test set. Small datasets require particular attention to model complexity and uncertainty. Classification reports should include class distributions, confusion matrices, sensitivity and specificity at a defined threshold, and confidence intervals, while regression reports should include prediction errors, bias, and performance across the calibration range. External-cohort testing, as illustrated by the EV and pathogen-classification examples [194,209], provides stronger evidence of transferability than randomly splitting repeated measurements from the same source.

Physics-informed approaches can complement data-driven models by incorporating governing equations and known material or spectral relationships [65–67]. In physics-informed neural networks (PINNs), residuals of electromagnetic equations and boundary conditions can be included in the training objective alongside available data. For inverse design, this formulation can support parameter retrieval and the search for structures with target optical responses. For spectral decoding, a reliable physical forward model may help constrain the inference of analyte properties, although parameter identifiability still

requires assessment. Material dispersion and fabrication constraints should also be considered. Physical consistency alone does not establish chemical specificity or robustness to unmodeled matrix effects; comparisons with simpler models, independent measurements, and uncertainty estimates remain necessary.

6.2. Reporting and Validation of Sensor Readiness

A common reporting framework should separate optical characterization, analytical validation, and evidence of operation in the intended setting. The following items are proposed as minimum reporting categories for research comparisons, rather than universal regulatory acceptance criteria.

Optical characterization should specify the measurement medium, illumination conditions, spectral resolution, resonance-fitting method, and uncertainty in Q, sensitivity, and FOM. Numerical values should be accompanied by the material model, analyte geometry, and simulation assumptions. Detection limits calculated or extrapolated from experimental data should be distinguished from the lowest concentrations tested, and the validated quantitative range should be reported separately from the full range of concentrations explored.

Analytical validation should include matrix-matched blanks, calibration details, and measurements near the proposed detection limit. The limit of blank describes the upper range of apparent signals expected from analyte-free samples, whereas the LOD describes the lowest analyte level distinguishable from the blank with a specified detection probability [249]. A 3σ-based estimate should state the source of σ, the calibration model, and whether the estimate was confirmed using low-concentration samples. Spike recovery should be evaluated at multiple concentration levels and calculated as Recovery = $[(C_{spiked} - C_{unspiked})/C_{added}] \times 100\%$, with all concentrations expressed on the same dilution-corrected basis. Cross-reactivity tests should include plausible interferents individually and in mixtures at relevant concentration ratios.

Precision reporting should distinguish repeated measurements within one chip, differences between chips, and differences between independently fabricated and functionalized batches. The corresponding numbers of independent units and technical replicates should be stated, together with RSD = s/mean × 100% where appropriate. Functionalization stability should be evaluated through retained target response, nonspecific background, and regeneration performance. Continuous operation requires an explicit observation period, baseline drift in signal units per unit time or concentration-equivalent units, and the temperature, humidity, flow, and matrix conditions. Storage stability and response retention after regeneration should be reported separately from operational drift.

Finally, claims of practical readiness should be supported by progressively more representative samples: controlled standards, matrix-spiked samples, independent real specimens, and operation in the intended clinical or environmental setting. Clinical classification requires independent subjects and comparison with relevant reference methods; environmental deployment requires evaluation across changing conditions, sampling sites, and measurement periods. Acceptance limits for recovery, precision, drift, and response time should be specified according to the intended application before validation, rather than imposed as a single threshold across all metasurface sensors.

Deployment requires integrated sampling, readout, calibration, and data transmission. Fiber-based, flexible, and portable designs offer useful routes, provided that packaging, interface lifetime, localized heating, and contamination are addressed. Automated sampling, regeneration, and wireless communication may further support sustained operation.

Author Contributions: Conceptualization, J.S.; investigation, J.B., L.J., T.D., Z.Z., Y.K., Y.W. and J.Z.; writing—original draft preparation, J.B., L.J., T.D., Z.Z., Y.K., Y.W. and J.Z.; visualization, T.D.;

writing—review and editing, J.S., H.D., F.W. and H.L.; supervision, J.S. and H.L.; project administration, J.S. and H.L. All authors have read and agreed to the published version of the manuscript.

Funding: This research was funded by the Research Start-up Fund for High-Level Talents of Heilongjiang University of Science and Technology (Grant No. HKDQDJ202675); the National Natural Science Foundation of China (Grant Nos. 52602251 and 62505351); the Basic Research Program of Jiangsu (Grant No. BK20250501); the Jiangsu Funding Program for Excellent Postdoctoral Talent (Grant No. 2025ZB653); the China Postdoctoral Science Foundation (Grant No. 2025M780548); and the Open Foundation of State Key Laboratory of Extreme Photonics and Instrumentation, Zhejiang University (Grant No. 2026EPIOP002).

Data Availability Statement: This article is a review and does not contain any new data. All data discussed in this article were obtained from previously published studies and have been cited accordingly.

Conflicts of Interest: The authors declare no conflicts of interest.

References

1. Dong, S.L.; He, D.; Zhang, Q.; Huang, C.N.; Hu, Z.H.; Zhang, C.Y.; Nie, L.; Wang, K.; Luo, W.; Yu, J.; et al. Early cancer detection by serum biomolecular fingerprinting spectroscopy with machine learning. *eLight* **2023**, *3*, 17. [CrossRef]
2. Wang, Y.; Ma, G.M.; Zheng, D.Y.; Jiang, J.; Yan, C. Gas Concentration Sensing Based on Fiber Loop Ring-Down Spectroscopy: A Review. *IEEE Trans. Instrum. Meas.* **2021**, *70*, 1–16. [CrossRef]
3. Ma, Y.F.; Sun, X.R.; Sun, H.Y.; He, Y.; Qiao, S.D. An ultra-highly sensitive LITES sensor based on multi-pass cell with ultra-dense spot pattern designed by multi-objective algorithm. *PhotoniX* **2025**, *6*, 26. [CrossRef]
4. Lin, D.; Liu, A.Q.; Pan, L.; Yang, L.; Jiang, C.L. Reversible flexible functional metal-organic frameworks sensor with artificial intelligence data analysis for real-time trace water monitor. *Chem. Eng. J.* **2025**, *526*, 170841. [CrossRef]
5. Kamel, A.H.; Abd-Rabboh, H.S.M.; Hefnawy, A. Molecularly imprinted polymer-based electrochemical sensors for monitoring the persistent organic pollutants chlorophenols. *RSC Adv.* **2024**, *14*, 20163–20181. [CrossRef]
6. Hanif, S.; Kousar, S.; Adil, N.; Akhtar, N.; Al-Sulami, A.I.; Khan, S.U.; Ahmed, A.; Yaqub, B.; Khan, M.A. Smart machine learning optimized electrochemical aptasensor for real-time monitoring of *Pseudomonas aeruginosa* in human saliva. *Microchem. J.* **2026**, *224*, 117651. [CrossRef]
7. Qiao, S.D.; Liu, X.N.; Lang, Z.T.; He, Y.; Chen, W.D.; Ma, Y.F. Quartz-enhanced laser spectroscopy sensing. *Light Sci. Appl.* **2026**, *15*, 5. [CrossRef]
8. Uniyal, A.; Srivastava, G.; Pal, A.; Taya, S.; Muduli, A. Recent Advances in Optical Biosensors for Sensing Applications: A Review. *Plasmonics* **2023**, *18*, 735–750. [CrossRef]
9. Wang, H.L.; You, E.M.; Panneerselvam, R.; Ding, S.Y.; Tian, Z.Q. Advances of surface-enhanced Raman and IR spectroscopies: From nano/microstructures to macro-optical design. *Light Sci. Appl.* **2021**, *10*, 161. [CrossRef]
10. Eslami, S.; Palomba, S. Integrated enhanced Raman scattering: A review. *Nano Converg.* **2021**, *8*, 41. [CrossRef]
11. Wen, Y.T.; Zhu, H.L.; Song, F.; Chen, R.T.; Zheng, C.T.; Pi, M.Q.; Zhang, Y.; Wang, Y.D. Surface-enhanced infrared absorption (SEIRA) based on Metasurface: Principles, biochemical sensing applications, and future perspective. *Spectrochim. Acta A Mol. Biomol. Spectrosc.* **2026**, *344*, 126621. [CrossRef]
12. Swinehart, D.F. The Beer-Lambert Law. *J. Chem. Educ.* **1962**, *39*, 333–335. [CrossRef]
13. Yu, X.T.; Yuan, Y.F.; Zhou, J.; Chang, M.; Zeng, S.W.; Zhuang, S.L. Sensitivity enhancement of surface plasmon resonance biosensors based on versatile nanostructures: Principle, fabrication, and illustrative applications. *Microsyst. Nanoeng.* **2026**, *12*, 45. [CrossRef]
14. Guo, C.P.; Liu, Z.Z.; He, Y.H.; Zhang, S.; He, L.H.; Wang, M.H.; Zhang, Z.H. Recent advances of surface plasmon resonance sensors based on metal-organic frameworks. *Talanta* **2025**, *292*, 128008. [CrossRef]
15. Lin, X.J.; Luo, Y.F.; Li, D.X.; Li, Y.; Gong, T.C.; Zhao, C.W.; Wang, C.T.; Duan, R.Q.; Yue, W.S. Recent advances in localized surface plasmon resonance (LSPR) sensing technologies. *Nanotechnology* **2025**, *36*, 202001. [CrossRef]
16. Bartolomé, M.; Villaseñor, M.J.; Ríos, A. Surface plasmon resonance optical sensors involving nanomaterials as reliable analytical tools: A critical view about performance and applications. *Anal. Chim. Acta* **2026**, *1382*, 344693. [CrossRef]
17. Luo, J.Y.; Sun, J.; Chen, H.C.; Zhao, C.L.; Ye, M.P. A Review of High-Sensitivity SERS-Active Photonic Crystal Fiber Sensors for Chemical and Biological Detection. *Sensors* **2025**, *25*, 6982. [CrossRef]
18. Chao, C.T.C.; Chau, Y.F.C. Engineering plasmonic photonic crystal fiber sensors: Design, fabrication strategies, and performance roadmap. *Mater. Sci. Eng. B* **2026**, *324*, 119046. [CrossRef]

19. Jiang, X.F.; Chang, L.; Zhang, J.; Wiersig, J.; Hentschel, M.; Wang, X.J.; Cao, H.; Xiao, Y.F.; Alù, A. Chaotic photonics in microresonators. *Nat. Rev. Phys.* **2026**, *8*, 365–382. [CrossRef]
20. Ansar, S.M.; Li, X.X.; Zou, S.L.; Zhang, D.M. Quantitative Comparison of Raman Activities, SERS Activities, and SERS Enhancement Factors of Organothiols: Implication to Chemical Enhancement. *J. Phys. Chem. Lett.* **2012**, *3*, 560–565. [CrossRef]
21. Hartstein, A.; Kirtley, J.R.; Tsang, J.C. Enhancement of the infrared absorption from molecular monolayers with thin metal overlayers. *Phys. Rev. Lett.* **1980**, *45*, 201–204. [CrossRef]
22. Neubrech, F.; Pucci, A.; Cornelius, T.W.; Karim, S.; García-Etxarri, A.; Aizpurua, J. Resonant Plasmonic and Vibrational Coupling in a Tailored Nanoantenna for Infrared Detection. *Phys. Rev. Lett.* **2008**, *101*, 157403. [CrossRef]
23. Lebrun, A.; Lavoie-Cardinal, F.; Boudreau, D. Surface-Enhanced Raman Spectroscopy Semi-Quantitative Molecular Profiling with a Convolutional Neural Network. *Appl. Spectrosc.* **2026**, *80*, 35–50. [CrossRef]
24. Yu, N.F.; Genevet, P.; Kats, M.A.; Aieta, F.; Tetienne, J.P.; Capasso, F.; Gaburro, Z. Light Propagation with Phase Discontinuities: Generalized Laws of Reflection and Refraction. *Science* **2011**, *334*, 333–337. [CrossRef]
25. Sievenpiper, D.; Zhang, L.J.; Broas, R.F.J.; Alexopoulos, N.G.; Yablonovitch, E. High-impedance electromagnetic surfaces with a forbidden frequency band. *IEEE Trans. Microw. Theory Tech.* **1999**, *47*, 2059–2074. [CrossRef]
26. Kazanskiy, N.L.; Khonina, S.N.; Butt, M.A. Recent Development in Metasurfaces: A Focus on Sensing Applications. *Nanomaterials* **2023**, *13*, 118. [CrossRef]
27. Li, C.; Gao, X.M.; Deng, X.Y.; Guo, J.Q.; Shen, C.; Zhang, Q. Merging bound states in the continuum-driven ultrahigh sensing figure of merit in all-dielectric metasurfaces. *Opt. Lett.* **2024**, *49*, 6469–6472. [CrossRef]
28. Jiang, T.; Bhattacharya, A.; Barkey, M.; Aigner, A.; Rohrer, L.; Weber, T.; Wang, J.; Maier, S.A.; Tittl, A. A Comparative Analysis of Plasmonic and Dielectric Metasurface Sensing Platforms Powered by Bound States in the Continuum. *Adv. Funct. Mater.* **2026**, *36*, e16021. [CrossRef]
29. Chen, S.N.; Gao, Y.; Sun, K.Y.; Zhang, Q.Y.; Ye, Z.H.; Fu, Q.H.; Fan, Y.C.; Zhang, F.L. Recent progress in Fano-resonant terahertz metasurface and its application. *Discov. Appl. Sci.* **2024**, *6*, 6. [CrossRef]
30. Wang, R.D.; Zhang, D.Z.; Chen, L.; Zhang, N.; Li, D.X.; Jiang, R.D.; Zhang, X.B.; Yang, X.; Zhang, L.Y.; Wang, S.M.; et al. Ultra-compact broadband terahertz spectroscopy sensor enabled by resonant-gradient metasurface. *Nat. Commun.* **2025**, *16*, 11462. [CrossRef]
31. Berger, L.M.; Duportal, M.; Menezes, L.d.S.; Cortés, E.; Maier, S.A.; Tittl, A.; Krischer, K. Improved In Situ Characterization of Electrochemical Interfaces Using Metasurface-Driven Surface-Enhanced IR Absorption Spectroscopy. *Adv. Funct. Mater.* **2023**, *33*, 2300411. [CrossRef]
32. Butt, M.A. Flatland Metasurfaces for Optical Gas Sensing. *Sensors* **2026**, *26*, 1293. [CrossRef]
33. Li, Q.; Yu, S.W.; Li, Z.C.; Liu, W.W.; Cheng, H.; Chen, S.Q. Metasurface-enhanced biomedical spectroscopy. *Nanophotonics* **2025**, *14*, 1045–1068. [CrossRef]
34. Hou, X.W.; Chen, T.H.; Wang, C.Y.; Liu, F.Y.; Zhao, M.G.; Ma, Y. Analyte mediated transformation of metasurface: A dual-mode plasmonic sensing platform for uric acid. *Talanta* **2026**, *298*, 129024. [CrossRef]
35. Muheki, J.; Wekalao, J.; Albargi, H.B.; Jalalah, M.; Almawgani, A.H.M.; Patel, S.K. A Graphene Gold Metasurface Inspired Surface Plasmon Resonance Sensor Designed for Terahertz Applications in Sensing and Detection of Heavy Metals in Water. *Plasmonics* **2025**, *20*, 289–303. [CrossRef]
36. Shen, L.L.; Liang, Y.Z.; Wei, X.R.; Wei, H.N.; Huang, Y.H.; Ju, F.Y.; He, Y.J.; Zhao, J.Y.; Yang, C.; Fang, Y.R.; et al. Aptamer-Driven Nanoparticles-Coupled Plasmonic Metasurface Biosensing Platform for Ultrasensitive and Quantitative Identification of Heavy Metal Cadmium Ions in Body Fluids. *ACS Sens.* **2025**, *10*, 4434–4441. [CrossRef]
37. Xiao, W.X.; Fan, X.Y.; Wang, Y.L.; Fang, W.J.; Sun, F.X.; Zhao, J.J.; Wei, X.; Li, C.C.; Tao, J.F.; Kumar, S. High-Q fano resonance metasurface sensor for refractive index and methane gas concentration measurement. *Opt. Commun.* **2025**, *574*, 131187. [CrossRef]
38. Li, R.; Zhou, Y.Z.; Chen, Y.Q.; Zhou, L.; Yang, Y.H.; Xiao, J.R.; Liu, G.L.; Wang, J.; Huang, L.P.; Li, Y.N. High-Electron-Mobility MXene-Enhanced Metasurface Biosensors Integrated with Microfluidics for Real-Time Multifunctional Monitoring. *ACS Nano* **2025**, *19*, 12007–12020. [CrossRef]
39. Zheng, W.J.; Meng, X.Y.; Ying, Q.Y.; Xin, Y.L.; Li, Z.Q.; Wang, M.Y.; Wu, C.S.; Wang, L.; Wang, T.L.; Yang, M.S.; et al. Graphene-Integrated Metasurface Terahertz Sensor Based on Toroidal Dipole Resonance for Ultrasensitive Pesticide Detection. *IEEE Trans. Terahertz Sci. Technol.* **2026**, *16*, 538–546. [CrossRef]
40. Yu, S.L.; Xu, M.F.; Pu, M.B.; Tang, X.; Zheng, Y.H.; Guo, Y.H.; Zhang, F.; Li, X.; Ma, X.L.; Luo, X.G. Dynamic nonlocal metasurface for multifunctional integration via phase-change materials. *Nanophotonics* **2024**, *13*, 4317–4325. [CrossRef]
41. Qin, J.; Jiang, S.B.; Wang, Z.S.; Cheng, X.B.; Li, B.J.; Shi, Y.Z.; Tsai, D.P.; Liu, A.Q.; Huang, W.; Zhu, W.M. Metasurface Micro/Nano-Optical Sensors: Principles and Applications. *ACS Nano* **2022**, *16*, 11598–11618. [CrossRef]
42. Tseng, M.L.; Jahani, A.; Leitis, A.; Altug, H. Dielectric Metasurfaces Enabling Advanced Optical Biosensors. *ACS Photonics* **2021**, *8*, 47–60. [CrossRef]

43. Barulin, A.; Nguyen, D.D.; Kim, Y.; Ko, C.H.; Kim, I. Metasurfaces for Quantitative Biosciences of Molecules, Cells, and Tissues: Sensing and Diagnostics. *ACS Photonics* **2024**, *11*, 904–916. [CrossRef]
44. Barbillon, G. Latest Advances in Metasurfaces for SERS and SEIRA Sensors as Well as Photocatalysis. *Int. J. Mol. Sci.* **2022**, *23*, 10592. [CrossRef]
45. Cui, T.J.; Zhang, S.; Alù, A.; Wegener, M.; Pendry, J.B.; Luo, J.; Lai, Y.; Wang, Z.; Lin, X.; Chen, H.; et al. Roadmap on electromagnetic metamaterials and metasurfaces. *J. Phys. Photonics* **2024**, *6*, 032502. [CrossRef]
46. Li, D.X.; Wu, X.Y.; Chen, Z.W.; Liu, T.; Mu, X.J. Surface-enhanced spectroscopy technology based on metamaterials. *Microsyst. Nanoeng.* **2025**, *11*, 36. [CrossRef]
47. Miroshnichenko, A.E.; Flach, S.; Kivshar, Y.S. Fano resonances in nanoscale structures. *Rev. Mod. Phys.* **2010**, *82*, 2257–2298. [CrossRef]
48. Koshelev, K.; Lepeshov, S.; Liu, M.K.; Bogdanov, A.; Kivshar, Y. Asymmetric Metasurfaces with High-Q Resonances Governed by Bound States in the Continuum. *Phys. Rev. Lett.* **2018**, *121*, 193903. [CrossRef]
49. Le Ru, E.C.; Etchegoin, P.G. *Principles of Surface-Enhanced Raman Spectroscopy: And Related Plasmonic Effects*; Elsevier: Amsterdam, The Netherlands, 2009; pp. 1–63.
50. Willets, K.A.; Van Duyne, R.P. Localized surface plasmon resonance spectroscopy and sensing. *Annu. Rev. Phys. Chem.* **2007**, *58*, 267–297. [CrossRef]
51. Bohren, C.F.; Huffman, D.R. *Absorption and Scattering of Light by Small Particles*; Wiley-VCH: Weinheim, Germany, 1998.
52. Yang, F.; Cao, W.; Zheng, G.C.; Qiu, L.; Nie, Z.H.; Li, Y. Plasmonic metasurfaces: Light-matter interactions, fabrication, applications and future outlooks. *Prog. Mater. Sci.* **2025**, *154*, 101508. [CrossRef]
53. Wang, X.; Huang, S.C.; Hu, S.; Yan, S.; Ren, B. Fundamental understanding and applications of plasmon-enhanced Raman spectroscopy. *Nat. Rev. Phys.* **2020**, *2*, 253–271. [CrossRef]
54. Kuznetsov, A.I.; Miroshnichenko, A.E.; Brongersma, M.L.; Kivshar, Y.S.; Luk'yanchuk, B. Optically resonant dielectric nanostructures. *Science* **2016**, *354*, aag2472. [CrossRef]
55. Jahani, S.; Jacob, Z. All-dielectric metamaterials. *Nat. Nanotechnol.* **2016**, *11*, 23–36. [CrossRef]
56. Decker, M.; Staude, I.; Falkner, M.; Dominguez, J.; Neshev, D.N.; Brener, I.; Pertsch, T.; Kivshar, Y.S. High-Efficiency Dielectric Huygens' Surfaces. *Adv. Opt. Mater.* **2015**, *3*, 813–820. [CrossRef]
57. Chung, T.R.; Wang, H.; Cai, H.G. Dielectric metasurfaces for next-generation optical biosensing: A comparison with plasmonic sensing. *Nanotechnology* **2023**, *34*, 402001. [CrossRef]
58. Luk'yanchuk, B.; Zheludev, N.I.; Maier, S.A.; Halas, N.J.; Nordlander, P.; Giessen, H.; Chong, C.T. The Fano resonance in plasmonic nanostructures and metamaterials. *Nat. Mater.* **2010**, *9*, 707–715. [CrossRef]
59. Chen, J.J.; Gan, F.Y.; Wang, Y.J.; Li, G.Z. Plasmonic Sensing and Modulation Based on Fano Resonances. *Adv. Opt. Mater.* **2018**, *6*, 1701152. [CrossRef]
60. Li, S.Y.; Zhou, C.B.; Liu, T.T.; Xiao, S.Y. Symmetry-protected bound states in the continuum supported by all-dielectric metasurfaces. *Phys. Rev. A* **2019**, *100*, 063803. [CrossRef]
61. Liang, Y.; Tsai, D.P.; Kivshar, Y. From Local to Nonlocal High-Q Plasmonic Metasurfaces. *Phys. Rev. Lett.* **2024**, *133*, 053801. [CrossRef]
62. Kivshar, Y. The Rise of Mie-tronics. *Nano Lett.* **2022**, *22*, 3513–3515. [CrossRef]
63. Kravets, V.G.; Kabashin, A.V.; Barnes, W.L.; Grigorenko, A.N. Plasmonic Surface Lattice Resonances: A Review of Properties and Applications. *Chem. Rev.* **2018**, *118*, 5912–5951. [CrossRef]
64. Lalanne, P.; Chen, M.; Rockstuhl, C.; Sprafke, A.; Dmitriev, A.; Vynck, K. Disordered optical metasurfaces: Basics, properties, and applications. *Adv. Opt. Photonics* **2025**, *17*, 45–112. [CrossRef]
65. Li, Z.Y.; Pestourie, R.; Lin, Z.; Johnson, S.G.; Capasso, F. Empowering Metasurfaces with Inverse Design: Principles and Applications. *ACS Photonics* **2022**, *9*, 2178–2192. [CrossRef]
66. Ji, W.Y.; Chang, J.; Xu, H.X.; Gao, J.R.; Gröblacher, S.; Urbach, H.P.; Adam, A.J.L. Recent advances in metasurface design and quantum optics applications with machine learning, physics-informed neural networks, and topology optimization methods. *Light Sci. Appl.* **2023**, *12*, 169. [CrossRef]
67. Jeong, J.Y.; Latif, S.; So, S. A Tutorial on Inverse Design Methods for Metasurfaces. *Curr. Opt. Photonics* **2024**, *8*, 531–544.
68. Schatz, G.C.; Young, M.A.; Van Duyne, R.P. Electromagnetic mechanism of SERS. In *Surface-Enhanced Raman Scattering: Physics and Applications*; Kneipp, K., Moskovits, M., Kneipp, H., Eds.; Springer: Berlin, Germany, 2006; Volume 103, pp. 19–45.
69. Hu, H.Y.; Pal, A.K.; Berestennikov, A.; Weber, T.; Stefancu, A.; Cortés, E.; Maier, S.A.; Tittl, A. Surface-Enhanced Raman Scattering in BIC-Driven Semiconductor Metasurfaces. *Adv. Opt. Mater.* **2024**, *12*, 2302812. [CrossRef]
70. Jayawardhana, S.; Rosa, L.; Juodkazis, S.; Stoddart, P.R. Additional Enhancement of Electric Field in Surface-Enhanced Raman Scattering due to Fresnel Mechanism. *Sci. Rep.* **2013**, *3*, 2335. [CrossRef]
71. Neubrech, F.; Huck, C.; Weber, K.; Pucci, A.; Giessen, H. Surface-Enhanced Infrared Spectroscopy Using Resonant Nanoantennas. *Chem. Rev.* **2017**, *117*, 5110–5145. [CrossRef]

72. Campion, A.; Kambhampati, P. Surface-enhanced Raman scattering. *Chem. Soc. Rev.* **1998**, *27*, 241–250. [CrossRef]
73. Kozuch, J.; Ataka, K.; Heberle, J. Surface-enhanced infrared absorption spectroscopy. *Nat. Rev. Methods Primers* **2023**, *3*, 70. [CrossRef]
74. Adato, R.; Altug, H. In-situ ultra-sensitive infrared absorption spectroscopy of biomolecule interactions in real time with plasmonic nanoantennas. *Nat. Commun.* **2013**, *4*, 2154. [CrossRef]
75. Pelton, M. Modified spontaneous emission in nanophotonic structures. *Nat. Photonics* **2015**, *9*, 427–435. [CrossRef]
76. Akselrod, G.M.; Argyropoulos, C.; Hoang, T.B.; Ciracì, C.; Fang, C.; Huang, J.N.; Smith, D.R.; Mikkelsen, M.H. Probing the mechanisms of large Purcell enhancement in plasmonic nanoantennas. *Nat. Photonics* **2014**, *8*, 835–840. [CrossRef]
77. Purcell, E.M. Spontaneous emission probabilities at radio frequencies. *Phys. Rev.* **1946**, *69*, 681.
78. Anger, P.; Bharadwaj, P.; Novotny, L. Enhancement and quenching of single-molecule fluorescence. *Phys. Rev. Lett.* **2006**, *96*, 113002. [CrossRef]
79. Liu, G.; Wang, Z.; Sun, W.; Lin, X.; Wang, R.; Li, C.; Zong, L.; Fu, Z.; Liu, H.; Xu, S. Robust emission in near-infrared II of lanthanide nanoprobes conjugated with Au (LNPs-Au) for temperature sensing and controlled photothermal therapy. *Chem. Eng. J.* **2023**, *452*, 139504. [CrossRef]
80. Anker, J.N.; Hall, W.P.; Lyandres, O.; Shah, N.C.; Zhao, J.; Van Duyne, R.P. Biosensing with plasmonic nanosensors. *Nat. Mater.* **2008**, *7*, 442–453. [CrossRef]
81. Mayer, K.M.; Hafner, J.H. Localized Surface Plasmon Resonance Sensors. *Chem. Rev.* **2011**, *111*, 3828–3857. [CrossRef]
82. Soler, M.; Huertas, C.S.; Lechuga, L.M. Label-free plasmonic biosensors for point-of-care diagnostics: A review. *Expert Rev. Mol. Diagn.* **2019**, *19*, 71–81. [CrossRef]
83. Yesilkoy, F.; Arvelo, E.R.; Jahani, Y.; Liu, M.K.; Tittl, A.; Cevher, V.; Kivshar, Y.; Altug, H. Ultrasensitive hyperspectral imaging and biodetection enabled by dielectric metasurfaces. *Nat. Photonics* **2019**, *13*, 390–396. [CrossRef]
84. Chen, W.J.; Li, M.; Zhang, W.H.; Chen, Y.H. Dual-resonance sensing for environmental refractive index based on quasi-BIC states in all-dielectric metasurface. *Nanophotonics* **2023**, *12*, 1147–1157. [CrossRef]
85. Iwanaga, M. All-Dielectric Metasurface Fluorescence Biosensors for High-Sensitivity Antibody/Antigen Detection. *ACS Nano* **2020**, *14*, 17458–17467. [CrossRef]
86. Kühner, L.; Sortino, L.; Berté, R.; Wang, J.; Ren, H.; Maier, S.A.; Kivshar, Y.; Tittl, A. Radial bound states in the continuum for polarization-invariant nanophotonics. *Nat. Commun.* **2022**, *13*, 4992. [CrossRef]
87. Johnson, S.G.; Ibanescu, M.; Skorobogatiy, M.A.; Weisberg, O.; Joannopoulos, J.D.; Fink, Y. Perturbation theory for Maxwell's equations with shifting material boundaries. *Phys. Rev. E* **2002**, *65*, 066611. [CrossRef]
88. Zhang, M.; Ge, C.; Lu, M.; Zhang, Z.; Cunningham, B.T. A self-referencing biosensor based upon a dual-mode external cavity laser. *Appl. Phys. Lett.* **2013**, *102*, 213701. [CrossRef]
89. Khan, S.A.; Khan, N.Z.; Xie, Y.N.; Abbas, M.T.; Rauf, M.; Mehmood, I.; Runowski, M.; Agathopoulos, S.; Zhu, J.F. Optical Sensing by Metamaterials and Metasurfaces: From Physics to Biomolecule Detection. *Adv. Opt. Mater.* **2022**, *10*, 2200500. [CrossRef]
90. Stuart, D.D.; Van Zant, W.; Valiulis, S.; Malinick, A.S.; Hanson, V.; Cheng, Q. Trends in surface plasmon resonance biosensing: Materials, methods, and machine learning. *Anal. Bioanal. Chem.* **2024**, *416*, 5221–5232. [CrossRef]
91. Shukla, S.; Arora, P. Aluminum as a competitive plasmonic material for the entire electromagnetic spectrum: A review. *Results Opt.* **2025**, *18*, 100760. [CrossRef]
92. Negm, A.; Howlader, M.M.R.; Belyakov, I.; Bakr, M.; Ali, S.; Irannejad, M.; Yavuz, M. Materials Perspectives of Integrated Plasmonic Biosensors. *Materials* **2022**, *15*, 7289. [CrossRef]
93. Otsuki, J.; Sugawa, K.; Jin, S. Plasmonic triangular nanoprism sensors. *Mater. Adv.* **2021**, *2*, 32–46. [CrossRef]
94. Montes-García, V.; Squillaci, M.A.; Diez-Castellnou, M.; Ong, Q.K.; Stellacci, F.; Samorì, P. Chemical sensing with Au and Ag nanoparticles. *Chem. Soc. Rev.* **2021**, *50*, 1269–1304. [CrossRef]
95. Hang, Y.J.; Wang, A.Y.; Wu, N.Q. Plasmonic silver and gold nanoparticles: Shape- and structure-modulated plasmonic functionality for point-of-caring sensing, bio-imaging and medical therapy. *Chem. Soc. Rev.* **2024**, *53*, 2932–2971. [CrossRef]
96. Karpinski, K.; Zielinska-Raczynska, S.; Ziemkiewicz, D. Aluminium-Based Plasmonic Sensors in Ultraviolet. *Sensors* **2021**, *21*, 4096. [CrossRef]
97. Mostufa, S.; Rezaei, B.; Ciannella, S.; Yari, P.; Gómez-Pastora, J.; He, R.; Wu, K. Advancements and Perspectives in Optical Biosensors. *ACS Omega* **2024**, *9*, 24181–24202. [CrossRef]
98. Huang, J.; Cheng, S. Six-band high-sensitivity terahertz absorption device based on AlCuFe quasicrystals for sensing applications. *Physica B* **2026**, *741*, 419152. [CrossRef]
99. Mao, X.; Li, H.; Gao, W.; Liu, M.; Li, B. Terahertz absorber with high sensitivity in triple bands based on AlCuFe. *Photonics Nanostruct. Fundam. Appl.* **2026**, *71*, 101566. [CrossRef]
100. Huang, X.; Chen, J.; Zhu, J.; Cheng, S.; Yi, Z.; Ahmad, S.; Tang, C.; Gao, F.; Li, B. Four-band narrowband terahertz metamaterial refractive index sensor with AlCuFe quasicrystal film for high-sensitivity biomedical monitoring applications. *Physica E* **2026**, *184*, 116629. [CrossRef]

101. Chen, X.E.; Xin, S.S.; Liu, Q.; Meng, Y.H.; Yu, D.Q.; Tseng, M.L.; Ye, L.F. Dielectric metasurface-assisted terahertz sensing: Mechanism, fabrication, and multiscenario applications. *Nanophotonics* **2025**, *14*, 271–296. [CrossRef]
102. Guo, H.Y.; Fang, W.J.; Pang, J.L.; Wang, T.T.; Fan, X.Y.; Huang, Y.Q.; Bai, C.L. Multiple fano resonances based on all-dielectric metastructure for refractive index sensing. *Infrared Phys. Technol.* **2024**, *139*, 105284. [CrossRef]
103. Zhao, J.J.; Fan, X.Y.; Fang, W.J.; Xiao, W.X.; Sun, F.X.; Bai, C.L.; Li, C.C.; Wei, X.; Kumar, S. Refractive index sensor based on bound states in the continuum in silicon-based metasurface. *Infrared Phys. Technol.* **2024**, *138*, 105189. [CrossRef]
104. Emani, N.K.; Khaidarov, E.; Paniagua-Domínguez, R.; Fu, Y.H.; Valuckas, V.; Lu, S.P.; Zhang, X.L.; Tan, S.T.; Demir, H.V.; Kuznetsov, A.I. High-efficiency and low-loss gallium nitride dielectric metasurfaces for nanophotonics at visible wavelengths. *Appl. Phys. Lett.* **2017**, *111*, 221101. [CrossRef]
105. Sulleiro, M.V.; Dominguez-Alfaro, A.; Alegret, N.; Silvestri, A.; Gómez, I.J. 2D Materials towards sensing technology: From fundamentals to applications. *Sens. Bio-Sens. Res.* **2022**, *38*, 100540. [CrossRef]
106. Rahman, M.T.; Kumar, R.; Kumar, M.; Qiao, Q.Q. Two-dimensional transition metal dichalcogenides and their composites for lab-based sensing applications: Recent progress and future outlook. *Sens. Actuators A Phys.* **2021**, *318*, 112517. [CrossRef]
107. Bi, H.; Yang, M.S.; You, R. Advances in terahertz metasurface graphene for biosensing and application. *Discov. Nano* **2023**, *18*, 63. [CrossRef]
108. Wei, Y.H.; Si, L.M.; Dong, L.; Shen, Q.T.; Ma, T.Y.; Sun, H.J.; Bao, X. A mid-IR tunable graphene metasurface for ultrasensitive molecular fingerprint retrieval and refractive index sensing. *J. Mater. Chem. C* **2023**, *11*, 16501–16508. [CrossRef]
109. Zha, Y.; Cheng, S. Tunable high-sensitivity mid-infrared perfect absorber with five resonance peaks based on nested circular and elliptical ring graphene surface plasmons. *Physica B* **2026**, *739*, 418929. [CrossRef]
110. Zhou, J.; Wang, C.; Zhang, X.H.; Jiang, L.; Wu, R.B. Advances in two-dimensional layered materials for gas sensing. *Mater. Sci. Eng. R Rep.* **2024**, *161*, 100872. [CrossRef]
111. Tang, X.; Hao, Q.; Hou, X.Y.; Lan, L.L.; Li, M.Z.; Yao, L.; Zhao, X.; Ni, Z.H.; Fan, X.C.; Qiu, T. Exploring and Engineering 2D Transition Metal Dichalcogenides toward Ultimate SERS Performance. *Adv. Mater.* **2024**, *36*, 2312348. [CrossRef]
112. Nawaz, M.Z.; Jiang, X.; Ahmad, W.; Li, M.; Zeng, Y.; Yang, X.; Li, P. Violet phosphorus: Synthesis, fundamental properties, and emerging applications. *Appl. Phys. Rev.* **2026**, *13*, 011324. [CrossRef]
113. Nawaz, M.Z.; Ahmad, W.; Hasan, I.M.U.; Gulzar, H.; Hasan, W.U.; Younis, U.; Farooq, A.; Saleem, M.S.; Li, M.; Chu, P.K. Modern 2D heterostructures: From fabrication challenges to emerging applications. *Small Methods* **2026**, *10*, e02365. [CrossRef]
114. Wu, Y.; Tao, W.W.; Zhao, F.F.; Li, C.X.; Fang, B.; Zhang, P.; Hong, Z.; Jing, X.F.; Yu, M.Z. Review for metamaterials and metasurfaces based on vanadium dioxide phase change materials. *Opt. Laser Technol.* **2024**, *179*, 111376. [CrossRef]
115. Fan, Z.H.; Deng, Q.L.; Ma, X.Y.; Zhou, S.L. Phase Change Metasurfaces by Continuous or Quasi-Continuous Atoms for Active Optoelectronic Integration. *Materials* **2021**, *14*, 1272. [CrossRef]
116. Zhang, C.; Ding, T. Active plasmonic nanodevices: From basic principles to emerging applications. *Responsive Mater.* **2024**, *2*, e20240024. [CrossRef]
117. Chen, Q.; Ye, Y.; Yu, T.; Guo, Z.; Nawaz, M.Z.; Yang, X.; Chen, H.; Deng, L.; Li, P. Laser-fabricated In_3SbTe_2 phase-change metasurfaces for infrared and terahertz polarization control. *ACS Photonics* **2026**, *13*, 3310–3318. [CrossRef]
118. Bhardwaj, S.K.; Singh, H.; Khatri, M.; Kim, K.H.; Bhardwaj, N. Advances in MXenes-based optical biosensors: A review. *Biosens. Bioelectron.* **2022**, *202*, 113995. [CrossRef]
119. Song, Y.; Sun, Z.S.; Kong, P.; Gui, H.; Li, Y.C.; Wang, Y.X.; Tang, J.G.; Huang, L.J. Recent advances in MXene based intelligent sensing. *Chem. Eng. J.* **2024**, *500*, 157305. [CrossRef]
120. He, K.; Ma, T. Carbon Dioxide Gas Sensor Based on Terahertz Metasurface with Asymmetric Cross-Shaped Holes Empowered by Quasi-Bound States in the Continuum. *Sensors* **2025**, *25*, 4178. [CrossRef]
121. Álvarez-Sanchis, J.A.; Vidal, B.; Díaz-Rubio, A. Huygens metasurface supporting quasi-bound states in the continuum for terahertz gas sensing. *Sci. Rep.* **2025**, *15*, 14504. [CrossRef]
122. Ghanim, A.M.; Alsayed, A.E.; Yahia, A.; Swillam, M.A. High Performance CO_2 Gas Sensing Using Plasmonic Bowtie and Fan-Shaped Nanoantennas. *ECS Sens. Plus* **2026**, *5*, 023401. [CrossRef]
123. Cao, Y.H.; Sun, H.S.; Song, X.B.; Feng, Z.H.; Liang, S.X.; Chen, Y.S.; Ma, L.J.; Li, L.Y.; Wu, W.G. A novel sandwich-type terahertz metasurface sensor integrated ultrathin microfluidic channel for direct detection of aqueous solutions. *Nanophotonics* **2025**, *14*, 2331–2343. [CrossRef]
124. Rosas, S.; Biswas, S.K.; Adi, W.; Kuruoglu, F.; Beisenova, A.; Patankar, M.S.; Yesilkoy, F. Mass-Manufactured Gradient Plasmonic Metasurfaces for Enhanced Mid-IR Spectrochemical Analysis of Complex Biofluids. *Adv. Mater.* **2025**, *37*, e04355. [CrossRef]
125. Wang, T.Y.; Jiang, Y.N.; Feng, H.Y.; Liu, L.L.; Deng, Q.S.; Liu, D.M.; Wang, C. Recent Advances in Raman Spectroscopy for Resolving Material Surfaces/Interfaces. *Catalysts* **2025**, *15*, 1131. [CrossRef]
126. Zhang, D.A.; Liu, X.; Zhao, Y.; Zhang, H.; Rudnev, A.V.; Li, J.F. In situ Raman spectroscopic studies of CO_2 reduction reactions: From catalyst surface structures to reaction mechanisms. *Chem. Sci.* **2025**, *16*, 4916–4936. [CrossRef]

127. Lu, W.J.; Jiang, Y.R.; Yao, X.B.; Yu, Y.; Shen, W.; Yang, M.; Huang, X.J.; Tang, X.H. Dispersive Pd islands-deposited Au nanorods for in situ SERS monitoring of catalytic reaction. *RSC Adv.* **2025**, *15*, 6663–6667. [CrossRef]
128. Hao, N.Y.; Luo, W.; Song, W.M.; Liu, K.Z.; Zhu, X.W.; Gu, J.; He, H.; Zhang, X.G.; Lu, Z.G.; Zhong, J.H. In Situ SERS Study of Electrocatalytic CO_2RR on Au@Pd Bimetallic Catalysts: From Isolated Single Atoms to Monolayer of Pd. *Aggregate* **2025**, *6*, e70190. [CrossRef]
129. Yang, W.P.; Geng, W.G.; Lu, X.Y.; Qian, L.H.; Luo, S.J.; Xu, L.; Shi, Y.; Song, T.D.; Li, M.Y. Unveiling the Photocatalytic Behavior of PNTP on Au-Ag Alloy Nanoshells Through SERS. *Catalysts* **2025**, *15*, 705. [CrossRef]
130. Saadatmand, S.B.; Ahmadi, V. Temperature-tunability of perovskite quasi-bound states in the continuum-metastructure for enhanced terahertz performance and CO2 sensing. *Sci. Rep.* **2025**, *15*, 26658. [CrossRef]
131. Zhang, R.; Liang, L.J.; Yan, X.; Wu, G.F.; Yao, H.Y.; Li, Z.H.; Hu, X.F.; Wang, Z.Q.; Sun, Z.Q.; Huang, J. Polyvinylpyrrolidone-enhanced terahertz metamaterials for room-temperature, trace VOC detection and discrimination. *Chem. Eng. J.* **2026**, *539*, 176936. [CrossRef]
132. Wang, L.; Zhang, B.; Dong, X.R.; Lu, Q.; Shen, H.; Ni, Y.; Liu, Y.C.; Song, H.T. Multi-Band Terahertz Metamaterial Absorber Integrated with Microfluidics and Its Potential Application in Volatile Organic Compound Sensing. *Electronics* **2025**, *14*, 2731. [CrossRef]
133. Zhao, J.; Wang, J.X. Quasi-Bound States in the Continuum-Enabled Wideband Terahertz Molecular Fingerprint Sensing Using Graphene Metasurfaces. *Nanomaterials* **2025**, *15*, 1178. [CrossRef]
134. Khafagy, M.; Ghanim, A.M.; Swillam, M.A. Tunable multi-band terahertz sensor based on graphene plasmonic metasurfaces. *Sci. Rep.* **2026**, *16*, 5938. [CrossRef]
135. Wertani, H.; Ben Krid, H.; Hlali, A.; Zairi, H. Graphene Integrated Terahertz Metasurface for Multi Gas Sensing Applications with Machine Learning Optimization. *Sens. Imaging* **2026**, *27*, 54. [CrossRef]
136. Meng, J.J.; Balendhran, S.; Sabri, Y.; Bhargava, S.K.; Crozier, K.B. Smart mid-infrared metasurface microspectrometer gas sensing system. *Microsyst. Nanoeng.* **2024**, *10*, 74. [CrossRef]
137. MoradiFotouhi, A.; Pourfath, M. Sensitive terahertz plasmonic metasurface biosensor integrated with microfluidics. *Nanoscale Adv.* **2025**, *7*, 4600–4609. [CrossRef]
138. Li, X.Y.; Wu, Z.B.; Zhang, Y.J.; Li, B. Terahertz metamaterial liquid detector optimized by deep learning. *Sci. Rep.* **2025**, *15*, 44825. [CrossRef]
139. Wekalao, J.; Elsayed, H.A.; Alqhtani, H.A.; Bin-Jumah, M.; Abukhadra, M.R.; Mehaney, A.; Rajakannu, A. High-sensitivity graphene-Ti3C2Tx metasurface for terahertz detection of formalin in aqueous environments with machine learning enhancement. *J. Mater. Sci.* **2025**, *60*, 23425–23446. [CrossRef]
140. Khodaie, A.; Rafighirani, Y.; Heidarzadeh, H.; Javidan, J.; Vasimalla, Y. High sensitivity formalin detection in aqueous solutions using plasmonic multifunctional metal insulator metal nanoring based optical refractive index sensor platform. *Sci. Rep.* **2026**, *16*, 10192. [CrossRef]
141. Gervais, T.; Jensen, K.F. Mass transport and surface reactions in microfluidic systems. *Chem. Eng. Sci.* **2006**, *61*, 1102–1121. [CrossRef]
142. Zhu, H.N.; Mesias, V.S.D.; Dai, X.; Qiu, W.T.; Yao, X.B.; Huang, J.Q. Simple strategy for preparing nanoporous silver sheets as reusable SERS substrates for trace analysis with up to 60 reuses. *Anal. Bioanal. Chem.* **2025**, *417*, 3611–3619. [CrossRef]
143. Singh, R.K.; Nirala, N.R.; Sadhasivam, S.; Muthukumar, D.; Sionov, E.; Shtenberg, G. Silver coated porous silicon microarray SERS platform for detecting aflatoxin B1 fumonisin B1 and ochratoxin A. *npj Sci. Food* **2025**, *9*, 165. [CrossRef]
144. Yan, F.C.; Zhang, R.; Wang, S.Q.; Zhang, N.; Zhang, X.Y. A pesticide residue detection model for food based on NIR and SERS. *PLoS ONE* **2025**, *20*, e0320456. [CrossRef]
145. Chen, Q.; Nie, H.; Liu, Q.K.; Tan, N.; Tuo, Z.; Yan, J.H.; Wen, L. Metasurface-engineered thermal emitters enabled chip-scale mid-infrared spectroscopic sensing. *PhotoniX* **2025**, *6*, 19. [CrossRef]
146. Gao, H.Y.; Liu, Y.Y.; Li, G.; Liu, H.D.; Shang, Y.X.; Ma, Z. On-Demand Design of Terahertz Metasurface Sensors for Detecting Plant Endogenous and Exogenous Molecules. *Agriculture* **2025**, *15*, 1481. [CrossRef]
147. Duportal, M.; Berger, L.M.; Maier, S.A.; Tittl, A.; Krischer, K. Multi-band Metasurface-Driven Surface-Enhanced Infrared Absorption Spectroscopy for Improved Characterization of in-Situ Electrochemical Reactions. *ACS Photonics* **2024**, *11*, 714–722. [CrossRef]
148. Wohlwend, J.; Wipf, O.; Kiwic, D.; Käch, S.; Mächler, B.; Haberfehlner, G.; Spolenak, R.; Galinski, H. CO_2 Conversion in Cu-Pd Based Disordered Network Metamaterials with Ultrasmall Mode Volumes. *Nano Lett.* **2025**, *25*, 3740–3746. [CrossRef]
149. Zhu, Z.J.; Qian, S.R.; Dong, X.D.; Liu, S.; Zhou, Y.X.; Nie, K.Q.; An, X.D.; Li, C.R.; Cheng, Y.; Yan, B.H.; et al. Light-induced pressurization effect in Au-Ni heterostructures for plasmonic photocatalysis. *Nat. Commun.* **2025**, *16*, 9560. [CrossRef]
150. Hu, S.; Goerlitzer, E.S.A.; Lin, Q.Q.; de Nijs, B.; Silkin, V.M.; Baumberg, J.J. Alchemically-glazed plasmonic nanocavities using atomic layer metals: Controllably synergizing catalysis and plasmonics. *Nat. Commun.* **2025**, *16*, 3370. [CrossRef]

151. Yang, J.J.; Chen, Z.; Wang, J.R.; Pan, B.C.; Zhang, Q.; Xiao, C.; Xie, Y. A localized surface plasmon resonance-interface induces ultrafast hot-electron spatiotemporal transfer for boosting photocatalytic H2 evolution integrated with benzylamine C-N coupling. *J. Mater. Chem. A* **2025**, *13*, 12159–12169. [CrossRef]
152. Wang, H. A repertoire of gold-based nanostructures with integrated optical and catalytic tunabilities. *Chem. Commun.* **2025**, *61*, 13807–13826. [CrossRef]
153. Poppe, A.; Lohia, I.; Osadchy, M.; Gibson, S.; de Nijs, B. Resolving Molecular Perturbations Near Undercoordinated Metals. *ACS Nano* **2025**, *19*, 20120–20127. [CrossRef]
154. Mai, Q.D.; Trang, D.T.H.; Loan, N.T.; Tran Thi, N.H.; Hoang, O.V.; Bach, T.N.; Hoa, N.Q.; Pham, A.T.; Le, A.T. Photo-induced-photo-catalytic SERS with silver-deposited TiO_2 nanorods for ultrasensitive and sustainable detection of low Raman cross-section molecules. *RSC Adv.* **2025**, *15*, 13172–13187. [CrossRef]
155. Mai, Q.D.; Trang, D.T.H.; Bach, T.N.; Le Na, V.T.; Pham, A.T.; Le, A.T. Synergizing PIERS and photocatalysis effects in a photo-responsive Ag/TiO2 nanostructure for an ultrasensitive and renewable PI-PC SERS technique. *RSC Adv.* **2025**, *15*, 4149–4162. [CrossRef]
156. Wang, R.N.; Wei, Y.J.; Li, G.Q.; Chen, S.Y.; Lin, J.; Hao, Q.; Fan, X.C.; Qiu, T. Beyond Plasmonics: Atomic-Scale SERS Platforms for Plasmon-Free Photocatalysis Monitoring via Charge Transfer Mechanisms. *Adv. Sens. Res.* **2025**, *4*, e00054. [CrossRef]
157. Turner, A.P.F. Biosensors: Sense and sensibility. *Chem. Soc. Rev.* **2013**, *42*, 3184–3196. [CrossRef]
158. Homola, J. Surface plasmon resonance sensors for detection of chemical and biological species. *Chem. Rev.* **2008**, *108*, 462–493. [CrossRef]
159. Kumar, S.; Singh, H.; Singh, D.K. Metasurfaces in Optical Biosensing: Revolutionizing Detection Techniques and Shaping the Future. *Photonics* **2025**, *12*, 360. [CrossRef]
160. Thomas, S.N.; French, D.; Jannetto, P.J.; Rappold, B.A.; Clarke, W.A. Liquid chromatography-tandem mass spectrometry for clinical diagnostics. *Nat. Rev. Methods Primers* **2022**, *2*, 96. [CrossRef]
161. Li, Y.S.; Zhang, G.Z.; Mao, X.; Yang, S.P.; De Ruyck, K.; Wu, Y.N. High sensitivity immunoassays for small molecule compounds detection—Novel noncompetitive immunoassay designs. *TrAC Trends Anal. Chem.* **2018**, *103*, 198–208. [CrossRef]
162. Cusano, A.M.; Quero, G.; Vaiano, P.; Cicatiello, P.; Principe, M.; Micco, A.; Ruvo, M.; Consales, M.; Cusano, A. Metasurface-assisted Lab-on-fiber optrode for highly sensitive detection of vitamin D. *Biosens. Bioelectron.* **2023**, *242*, 115717. [CrossRef]
163. Fan, H.L.; Li, R.; Chen, Y.Q.; Da, Q.; Xiong, C.C.; Zhang, Y.Y.; Qin, Z.G.; Liu, G.L.; Huang, L.P. Sample-to-answer point-of-care testing platform for quantitative detection of small molecules in blood using a smartphone-and microfluidic-based nanoplasmonic biosensor. *Chem. Eng. J.* **2024**, *501*, 157495. [CrossRef]
164. Li, R.; Fan, H.L.; Chen, Y.Q.; Yin, S.P.; Liu, G.L.; Li, Y.N.; Huang, L.P. MXene-Graphene Oxide Heterostructured Films for Enhanced Metasurface Plasmonic Biosensing in Continuous Glucose Monitoring. *Adv. Sci.* **2025**, *12*, 2410376. [CrossRef]
165. Li, Y.; Liu, W.; Liu, R.; Gao, J.; Feng, J.; Xu, S.; Li, Z.; Jiang, S.; Du, X. 3D hybrid arrayed Ag/MOF multi-plasmon resonant cavity system for high-performance SPR sensing. *Opt. Laser Technol.* **2023**, *167*, 109825. [CrossRef]
166. She, S.C.; Zuo, J.C.; Li, Y.; Sun, L.; Yang, Z.K.; Dai, Y.W.; Yang, F.; Zhang, Y.Z.; He, M.X. Terahertz metasurface biosensor empowered by quasi-bound states in the continuum for label-free identification of different cancers and trace molecular sensing. *Chem. Eng. J.* **2025**, *520*, 165634. [CrossRef]
167. Niu, Q.; He, K.; Zhao, R.; Xie, Y.N.; Murtaza, G.; Zhang, G.L.; Xiao, S.Q.; Zeng, F.; Yang, Y.P.; Zhu, J.F. Broadband-Enhanced Terahertz Metasurface Biosensor Enables Molecular Fingerprint Trace Detection via Single-Shot Acquisition. *ACS Photonics* **2025**, *12*, 5939–5947. [CrossRef]
168. Zheng, P.; Semancik, S.; Barman, I. Deep Learning-Assisted SERS for Therapeutic Drug Monitoring of Clozapine in Serum on Plasmonic Metasurfaces. *Nano Lett.* **2025**, *25*, 5342–5349. [CrossRef]
169. Wang, Y.L.; Zhao, C.; Wang, J.J.; Luo, X.; Xie, L.J.; Zhan, S.J.; Kim, J.; Wang, X.Z.; Liu, X.J.; Ying, Y.B. Wearable plasmonic-metasurface sensor for noninvasive and universal molecular fingerprint detection on biointerfaces. *Sci. Adv.* **2021**, *7*, eabe4553. [CrossRef]
170. Zhu, H.L.; Fohlerová, Z.; Pekárek, J.; Basova, E.; Neuzil, P. Recent advances in lab-on-a-chip technologies for viral diagnosis. *Biosens. Bioelectron.* **2020**, *153*, 112041. [CrossRef]
171. Arya, M.; Shergill, I.S.; Williamson, M.; Gommersall, L.; Arya, N.; Patel, H.R.H. Basic principles of real-time quantitative PCR. *Expert Rev. Mol. Diagn.* **2005**, *5*, 209–219. [CrossRef]
172. Hu, J.; Safir, F.; Chang, K.; Dagli, S.; Balch, H.B.; Abendroth, J.M.; Dixon, J.; Moradifar, P.; Dolia, V.; Sahoo, M.K.; et al. Rapid genetic screening with high quality factor metasurfaces. *Nat. Commun.* **2023**, *14*, 4486. [CrossRef]
173. Yu, Z.C.; Pan, L.; Ma, X.W.; Li, T.M.; Wang, F.K.; Yang, D.L.; Li, M.; Wang, P.F. Detection of SARS-CoV-2 RNA with a plasmonic chiral biosensor. *Biosens. Bioelectron.* **2023**, *237*, 115526. [CrossRef]
174. Li, Y.M.; Wang, X.J.; Liu, Y.; Jin, W.D.; Tian, H.Y.; Xie, F.X.; Xia, K.; Zhang, X.M.; Fu, W.L.; Zhang, Y. Flexible Terahertz Metamaterial Biosensor for Ultra-Sensitive Detection of Hepatitis B Viral DNA Based on the Metal-Enhanced Sandwich Assay. *Front. Bioeng. Biotechnol.* **2022**, *10*, 930800. [CrossRef]

175. Luo, X.Z.; Li, J.N.; Huang, G.R.; Xie, F.X.; He, Z.; Zeng, X.J.; Tian, H.Y.; Liu, Y.; Fu, W.L.; Yang, X. Metal-Graphene Hybrid Terahertz Metasurfaces for Circulating Tumor DNA Detection Based on Dual Signal Amplification. *ACS Sens.* **2024**, *9*, 2122–2133. [CrossRef]
176. Iwanaga, M. Single-MicroRNA Detection on High-Selectivity Metasurface Fluorescence Biosensors. *ACS Nano* **2025**, *19*, 38841–38848. [CrossRef]
177. Shi, W.; Fan, F.; Zhang, J.; Zhang, L.; Xiao, G.H.; Ren, Z.; Zhao, J.L.; Wang, X.H. Terahertz Let-7a specific sensing and DNA differentiation enabled by Q-BIC metasurface and phenylboronic acid-gold nanoprobe. *Talanta* **2026**, *297*, 128577. [CrossRef]
178. Zhao, L.X.; Sun, L.; Chu, X.G. Chemiluminescence immunoassay. *TrAC Trends Anal. Chem.* **2009**, *28*, 404–415. [CrossRef]
179. Tabatabaei, M.S.; Islam, R.; Ahmed, M. Applications of gold nanoparticles in ELISA, PCR, and immuno-PCR assays: A review. *Anal. Chim. Acta* **2021**, *1143*, 250–266. [CrossRef]
180. Li, R.; Fan, H.L.; Zhou, H.L.; Chen, Y.Q.; Yu, Q.C.; Hu, W.J.; Liu, G.L.; Huang, L.P. Nanozyme-Catalyzed Metasurface Plasmon Sensor-Based Portable Ultrasensitive Optical Quantification Platform for Cancer Biomarker Screening. *Adv. Sci.* **2023**, *10*, 2301658. [CrossRef]
181. Liang, H.T.; Wang, X.G.; Li, F.J.; Xie, Y.N.; Shen, J.Q.; Wang, X.Q.; Huang, Y.Q.; Lin, S.W.; Chen, J.J.; Zhang, L.J.; et al. Label-free plasmonic metasensing of PSA and exosomes in serum for rapid high-sensitivity diagnosis of early prostate cancer. *Biosens. Bioelectron.* **2023**, *235*, 115380. [CrossRef]
182. Iwanaga, M. Robust Detection of Cancer Markers in Human Serums Using All-Dielectric Metasurface Biosensors. *Biosensors* **2023**, *13*, 377. [CrossRef]
183. Zhu, J.F.; Wang, Z.Y.; Lin, S.W.; Jiang, S.; Liu, X.Y.; Guo, S.S. Low-cost flexible plasmonic nanobump metasurfaces for label-free sensing of serum tumor marker. *Biosens. Bioelectron.* **2020**, *150*, 111905. [CrossRef]
184. Wang, T.L.; Li, Z.Q.; Wang, M.Y.; Wu, C.S.; Yang, M.S.; Yang, X.W.; Wang, L.; Li, K.L.; Yang, Z.; Zheng, W.J.; et al. Trace protein detection by graphene-integrated terahertz meta-sensor and enhanced sensitivity using gold nanoparticles-assisted. *Biosens. Bioelectron.* **2025**, *286*, 117612. [CrossRef]
185. Wu, J.; Chen, Y.Q.; Huang, L.P.; Sun, Y.H.; Zhao, J.J.; Cheng, X.Y.; Sun, R.W.; Zhou, H.L.; Shu, Y.; Li, W.; et al. High-throughput real-time detection of sepsis inflammatory biomarker proteins in clinical samples using metasurface plasmon resonance biosensors. *Chem. Eng. J.* **2025**, *522*, 167829. [CrossRef]
186. Wang, R.; Xu, L.; Huang, L.J.; Zhang, X.B.; Ruan, H.; Yang, X.; Lou, J.; Chang, C.; Du, X.H. Ultrasensitive Terahertz Biodetection Enabled by Quasi-BIC-Based Metasensors. *Small* **2023**, *19*, 2301165. [CrossRef]
187. Karthikeyan, N.; Bhargav, J.; Karthik, S.; Kavitha, M.S. Ultrasensitive Detection and Spectral Analysis of Protein Biomarkers Using 3D Nanopillar SERS Platforms with Tunable Hotspots. *Plasmonics* **2026**, *21*, 1361–1375. [CrossRef]
188. Zheng, P.; Wu, L.T.; Raj, P.; Kim, J.H.; Paidi, S.K.; Semancik, S.; Barman, I. Multiplexed SERS Detection of Serum Cardiac Markers Using Plasmonic Metasurfaces. *Adv. Sci.* **2024**, *11*, 2405910. [CrossRef]
189. Kim, M.; Kang, D.H.; Choi, J.H.; Choi, D.G.; Lee, J.; Lee, J.; Jung, J.Y. Highly sensitive and label-free protein immunoassay-based biosensor comprising infrared metamaterial absorber inducing strong coupling. *Biosens. Bioelectron.* **2024**, *260*, 116436. [CrossRef]
190. Kim, H.; Yun, H.; Jeong, S.; Ryu, M.; Jang, J.; Jung, C.; Yang, Y.; Lee, E.; Jeong, M.; Ryu, Y.S.; et al. Direct imaging-based gradient metasurface sensor enabling spectrometer-free ultrasensitive biomolecule detection. *Nat. Commun.* **2026**, *17*, 7900. [CrossRef]
191. Böing, A.N.; van der Pol, E.; Grootemaat, A.E.; Coumans, F.A.W.; Sturk, A.; Nieuwland, R. Single-step isolation of extracellular vesicles by size-exclusion chromatography. *J. Extracell. Vesicles* **2014**, *3*, 23430. [CrossRef]
192. Welsh, J.A.; Goberdhan, D.C.I.; O'Driscoll, L.; Buzas, E.I.; Blenkiron, C.; Bussolati, B.; Cai, H.; Di Vizio, D.; Driedonks, T.A.P.; Erdbrügger, U.; et al. Minimal information for studies of extracellular vesicles (MISEV2023): From basic to advanced approaches. *J. Extracell. Vesicles* **2024**, *13*, e12404. [CrossRef]
193. Shen, J.Q.; Wang, X.G.; Li, F.J.; Zhu, J.H.; Gao, Y.; Chen, K.B.; Huang, Y.Q.; Zhang, L.J.; Luo, Y.; Jiang, B.L.; et al. Volume-oriented meta-plasmonic sensing of serum extracellular vesicles for rapid kidney cancer diagnosis and monitoring. *Sens. Actuators B Chem.* **2026**, *446*, 138756. [CrossRef]
194. Zhu, J.H.; Xiao, Y.Q.; Huang, X.Y.; Niu, Q.; Zeng, L.H.; Lin, S.W.; Jiang, M.Q.; Huang, T.H.; Chen, H.Y.; Xie, Y.N.; et al. Deep Learning-Powered Nanoplasmonic Biosensing Approach Enables Ultrasensitive Extracellular Vesicles Profiling for Cancer Screening. *Adv. Sci.* **2026**, *13*, e11337. [CrossRef]
195. Hu, R.S.; Lin, S.W.; Li, F.J.; Shen, J.Q.; Xie, Y.N.; Deng, B.C.; Zhang, Y.Y.; Dong, Z.G.; Zhu, J.F. Exploring Aptamer-Based Metasurfaces for Label-Free Plasmonic Biosensing of Breast Tumor-Derived Exosomes. *Adv. Opt. Mater.* **2024**, *12*, 2401180. [CrossRef]
196. Bao, H.M.; Tan, E.X.; Zhou, J.; Zhao, X.; Leong, S.Y.; Chek, C.H.; Leon, G.K.; Chen, J.R.T.; Nguyen, L.B.T.; Li, L.; et al. From hotspots to hotspaces: Cascaded photonic-plasmonic coupling for SERS-based deep profiling of whole small extracellular vesicles. *Sci. Adv.* **2026**, *12*, eaec1846. [CrossRef]
197. Hong, C.C.; Hong, I.K.; Yang, S.; Ndukaife, J.C. Towards rapid colorimetric detection of extracellular vesicles using optofluidics-enhanced color-changing optical metasurface. *Opt. Express* **2024**, *32*, 4769–4777. [CrossRef]

198. Li, Y.M.; Wang, P.L.; Li, W.Y.; Li, Z.R.; Ji, F.Y.; Ma, Q. Plasmonic-photonic metasensor with mesoporous Nb_2C MXene for the detection of IgAN extracellular vesicles. *Biosens. Bioelectron.* **2026**, *292*, 118068. [CrossRef]
199. Shrivastav, A.M.; Cvelbar, U.; Abdulhalim, I. A comprehensive review on plasmonic-based biosensors used in viral diagnostics. *Commun. Biol.* **2021**, *4*, 70. [CrossRef]
200. Ahmed, R.; Guimarães, C.F.; Wang, J.; Soto, F.; Karim, A.H.; Zhang, Z.W.; Reis, R.L.; Akin, D.; Paulmurugan, R.; Demirci, U. Large-Scale Functionalized Metasurface-Based SARS-CoV-2 Detection and Quantification. *ACS Nano* **2022**, *16*, 15946–15958. [CrossRef]
201. Zhang, Q.M.; Rawal, G.; Qian, J.J.; Zou, S.P.; Gillingham, J.; Zhang, J.Q.; Dong, L.; Lu, M. Hybrid Metasurface for On-Chip Enrichment and Quantification of Biological Samples. *ACS Appl. Mater. Interfaces* **2025**, *17*, 22464–22473. [CrossRef]
202. Li, Z.L.; Xie, M.X.; Nie, G.Z.; Wang, J.H.; Huang, L.J. Pushing Optical Virus Detection to a Single Particle through a High-Q Quasi-bound State in the Continuum in an All-dielectric Metasurface. *J. Phys. Chem. Lett.* **2023**, *14*, 10762–10768. [CrossRef]
203. Ji, G.S.; Kim, H.S.; Cha, S.H.; Lee, H.T.; Kim, H.J.; Lee, S.W.; Ahn, K.J.; Kim, K.H.; Ahn, Y.H.; Park, H.R. Terahertz virus-sized gold nanogap sensor. *Nanophotonics* **2023**, *12*, 147–154. [CrossRef]
204. Amin, M.; Siddiqui, O.; Abutarboush, H.; Farhat, M.; Ramzan, R. A THz graphene metasurface for polarization selective virus sensing. *Carbon* **2021**, *176*, 580–591. [CrossRef]
205. Garg, A.; Zong, Z.; Vikesland, P.; Gloag, E.S.; Zhou, W. Zwitterionic nanoplasmonic bio-meshes for in situ spatiotemporal SERS monitoring of *Pseudomonas aeruginosa* biofilms. *npj Biosens.* **2025**, *2*, 30. [CrossRef]
206. Rajapaksha, P.; Elbourne, A.; Gangadoo, S.; Brown, R.; Cozzolino, D.; Chapman, J. A review of methods for the detection of pathogenic microorganisms. *Analyst* **2019**, *144*, 396–411. [CrossRef]
207. Kabiraz, M.P.; Majumdar, P.R.; Mahmud, M.M.C.; Bhowmik, S.; Ali, A. Conventional and advanced detection techniques of foodborne pathogens: A comprehensive review. *Heliyon* **2023**, *9*, e15482. [CrossRef]
208. Zhong, H.; Li, J.L.; Jiang, J.H.; Xu, X.P.; Zhang, D.D.; Song, L.W.; Gao, R.; Tian, Y. Label-free sensing technology of two *Staphylococcus* species based on a terahertz metasurface. *Biomed. Opt. Express* **2025**, *16*, 2210–2216. [CrossRef]
209. Yu, W.J.; Long, Y.P.; Luo, J.J.; Zhou, D.H.; Fan, C.; Ren, Y.T.; Shi, J.; Huang, Q.; Yang, X. Machine Learning-Assisted Terahertz Metagrating Biosensor for Label-Free Bacterial Identification Based on Spectral Fingerprinting. *Anal. Chem.* **2025**, *97*, 22164–22173. [CrossRef]
210. Meng, Q.H.; Zhao, Y.H.; Wang, X.Y.; Su, B.; Zhang, S.B.; Cui, H.L.; Zhang, C.L. Highly integrated automatic injection terahertz microfluidic biosensor based on metasurface and LT-GaAs photoconductive antenna. *Opt. Express* **2024**, *32*, 16867–16878. [CrossRef]
211. Ma, J.L.; Wang, J.J.; He, H.; Ling, F.; Huang, Y.Z.; Wu, X.X.; Li, S.B.; Xu, Y.; Wang, L.; Yang, X. Rapid and Early Detection of Bacteremia and In Situ Elimination by Graphene Hybrid Terahertz Metasurfaces with CuS Nanoparticles. *ACS Nano* **2025**, *19*, 28588–28601. [CrossRef]
212. Kurt, H.; Soylukan, C.; Çelik, S.; Çapkin, E.; Acuner, I.C.; Topkaya, A.E.; Yüce, M. Rapid and sensitive biosensing of uropathogenic E. coli using plasmonic nanohole arrays on MIM: Bridging the gap between lab and clinical diagnostics. *Biosens. Bioelectron.* **2025**, *280*, 117419. [CrossRef]
213. Adan, A.; Kiraz, Y.; Baran, Y. Cell Proliferation and Cytotoxicity Assays. *Curr. Pharm. Biotechnol.* **2016**, *17*, 1213–1221. [CrossRef]
214. Srinivasan, B.; Kolli, A.R.; Esch, M.B.; Abaci, H.E.; Shuler, M.L.; Hickman, J.J. TEER Measurement Techniques for In Vitro Barrier Model Systems. *JALA* **2015**, *20*, 107–126. [CrossRef]
215. Chen, Y.Q.; Li, W.; Feng, J.Y.; Shu, Y.; Yang, Y.H.; Wang, Y.Y.; Li, R.; Zhou, H.L.; Yang, X.F.; Guo, Y.X.; et al. Innovative Metasurface Colorimetric Cell-on-a-Chip Sensor for Continuous, Label-Free, Non-Destructive Assessment of Intestinal Barrier Dynamics. *Adv. Sci.* **2026**, *13*, e23118. [CrossRef]
216. Chen, M.Q.; Li, W.; Hu, T.Y.; Chang, J.X.; Chen, Y.Q.; Yang, Y.H.; Liu, G.L.; Hu, W.J. Meta-surface plasmon resonance microscopy for sensitive, high-throughput, and long-term label-free analysis of cell adhesion dynamics. *J. Nanobiotechnol.* **2025**, *23*, 752. [CrossRef]
217. Li, W.; Chen, M.Q.; Chen, Y.Q.; Yang, Y.H.; Ruan, J.Y.; Chang, J.X.; Li, J.C.; Liu, G.L.; Hu, W.J. Metasurface plasmon resonance platform for high-throughput, label-free, real-time, long-term monitoring of in vitro cancer therapy assessment. *Biosens. Bioelectron.* **2026**, *292*, 118052. [CrossRef]
218. Liu, H.; Ke, X.; Shen, L.R.; Cao, Y.Q.; Huang, W.; Tian, L.F.; Zhang, Y.; Huang, P.J.; Zhang, G.X. Bilayer terahertz metasurface with ultra-high Q factor for tumor chemosensitivity sensing. *Chem. Eng. J.* **2026**, *539*, 177266. [CrossRef]
219. Zhao, Z.Y.; Xue, Y.H.; Yang, J.; Qin, H.; Yang, X.T. Identification of macrophage polarization phenotypes in agarose matrix using metasurface-based terahertz biosensor of quasi-bound state continuum. *Appl. Phys. Lett.* **2023**, *123*, 183701. [CrossRef]
220. Roh, Y.; Kwak, J.; Sim, S.J.; Song, H.S.; Seo, M. Investigating the Potential for Label-Free Detection of Cell Apoptosis through Terahertz Nano-Metasurfaces. *Adv. Photon. Res.* **2025**, *6*, 2400166. [CrossRef]
221. Han, L.L.; Wang, Y.C.; Chen, K.L.; Gao, H.Y.; Xia, K.X.; Ge, Q.G.; Yang, J.; Shi, W.; Ruan, C.J. Detection of In Vivo-like Cells by a Biosensor Chip Based on Metamaterials in Terahertz Regime. *Biosensors* **2024**, *14*, 230. [CrossRef]

222. Mahalanabish, A.; Huang, S.H.; Tulegenov, D.; Shvets, G. Infrared Spectroscopy of Live Cells Using High-Aspect-Ratio Metal-on-Dielectric Metasurfaces. *Nano Lett.* **2024**, *24*, 11607–11614. [CrossRef]
223. Kelp, G.; Li, J.; Lu, J.L.; DiNapoli, N.; Delgado, R.; Liu, C.; Fan, D.; Dutta-Gupta, S.; Shvets, G. Infrared spectroscopy of live cells from a flowing solution using electrically-biased plasmonic metasurfaces. *Lab Chip* **2020**, *20*, 2136–2153. [CrossRef]
224. Niccolini, B.; Di Santo, R.; Mazzinelli, E.; Orlando, M.; Russo, A.; Ortolani, M.; Di Gaspare, A.; Rosa, E.; Notargiacomo, A.; Pea, M.; et al. Dual-mode mid-infrared plasmonic metasurface for real-time label-free analysis of live cells. *Talanta* **2026**, *301*, 129240. [CrossRef]
225. Wang, Q.T.; Wang, Z.Q.; Wang, C.Z.; Tian, H.H.; Qi, Y.H.; Yan, X.; Zhao, R.R.; Li, B.Y.; Ma, C.Z.; Xin, T.; et al. Slope Extrusion Microchannel Integrating Terahertz Meta-Sensor Embedded in Cerebrospinal Fluid for Precise Diagnosis of PCNSIs. *ACS Sens.* **2025**, *10*, 7549–7558. [CrossRef]
226. Shen, P.; Ji, Y.Y.; Yue, X.M.; Li, Y.F.; Han, M.F.; Ma, Y.; Meng, M.; Fan, F.; Chang, S.J. Ultrasensitive terahertz microfluidic biosensor integrated with tetrahedral DNA nanostructure for specific detection of live cancer cells. *Sens. Actuators B Chem.* **2025**, *428*, 137252. [CrossRef]
227. La Spada, L. Metasurfaces for Advanced Sensing and Diagnostics. *Sensors* **2019**, *19*, 355. [CrossRef]
228. Ullah, N.; Zhao, R.Z.; Huang, L.L. Recent Advancement in Optical Metasurface: Fundament to Application. *Micromachines* **2022**, *13*, 1025. [CrossRef]
229. Nugroho, F.A.A.; Bai, P.; Darmadi, I.; Castellanos, G.W.; Fritzsche, J.; Langhammer, C.; Gómez Rivas, J.; Baldi, A. Inverse designed plasmonic metasurface with parts per billion optical hydrogen detection. *Nat. Commun.* **2022**, *13*, 5737. [CrossRef]
230. Cai, S.S.; Hu, W.H.; Liu, Y.M.; Ning, J.; Feng, S.X.; Jin, C.; Huang, L.L.; Li, X. Optical fiber hydrogen sensor using metasurfaces composed of palladium. *Chin. Opt. Lett.* **2022**, *20*, 053601. [CrossRef]
231. Tan, X.C.; Zhang, H.; Li, J.Y.; Wan, H.W.; Guo, Q.S.; Zhu, H.B.; Liu, H.; Yi, F. Non-dispersive infrared multi-gas sensing via nanoantenna integrated narrowband detectors. *Nat. Commun.* **2020**, *11*, 5245. [CrossRef]
232. Kim, I.; Kim, W.S.; Kim, K.; Ansari, M.A.; Mehmood, M.Q.; Badloe, T.; Kim, Y.; Gwak, J.; Lee, H.; Kim, Y.K.; et al. Holographic metasurface gas sensors for instantaneous visual alarms. *Sci. Adv.* **2021**, *7*, eabe9943. [CrossRef]
233. Liu, Y.; Li, X.W.; Chen, Y.F.; Geng, G.Z.; Li, J.J.; Wang, Y.T.; Huang, L.L. Imaging-based optical barcoding for relative humidity sensing based on meta-tip. *Nanophotonics* **2022**, *11*, 111–118. [CrossRef]
234. Xing, W.Q.; Bian, X.M.; Su, R.G.; Han, Y.K.; Li, T.S.; You, R. Direct Aerosol Detection of SARS-CoV-2 S Protein Using a Terahertz Metasurface Sensor Based on Bound States in the Continuum. *ACS Appl. Mater. Interfaces* **2026**, *18*, 4865–4874. [CrossRef]
235. Almawgani, A.H.M.; Surve, J.; Parmar, T.; Armghan, A.; Aliqab, K.; Ali, G.A.; Patel, S.K. A Graphene-Metasurface-Inspired Optical Sensor for the Heavy Metals Detection for Efficient and Rapid Water Treatment. *Photonics* **2023**, *10*, 56. [CrossRef]
236. Li, R.L.; Wang, Z.; Zhang, Z.P.; Sun, X.T.; Hu, Y.Y.; Wang, H.Y.; Chen, K.C.; Liu, Q.; Chen, M.; Chen, X.Q. Deep Learning-Based Multicapturer SERS Platform on Plasmonic Nanocube Metasurfaces for Multiplex Detection of Organophosphorus Pesticides in Environmental Water. *Anal. Chem.* **2022**, *94*, 16006–16014. [CrossRef]
237. Bdour, Y.; Beaton, G.; Gomez-Cruz, J.; Cabezuelo, O.; Stamplecoskie, K.; Escobedo, C. Hybrid plasmonic metasurface as enhanced Raman hot-spots for pesticide detection at ultralow concentrations. *Chem. Commun.* **2023**, *59*, 8536–8539. [CrossRef]
238. Ma, B.Z.; Ouyang, A.; Zhong, J.C.; Belov, P.A.; Sinha, R.K.; Qian, W.P.; Ghosh, P.; Li, Q. All-Dielectric Metasurface for Sensing Microcystin-LR. *Electronics* **2021**, *10*, 1363. [CrossRef]
239. Ece, E.; Aslan, Y.; Haciosmanoglu, N.; Inci, F. MicroMetaSense: Coupling Plasmonic Metasurfaces with Fluorescence for Enhanced Detection of Microplastics in Real Samples. *ACS Sens.* **2025**, *10*, 725–740. [CrossRef]
240. Sperling, J.R.; Poursat, B.; Savage, L.; Christie, I.; Cuthill, C.; Aekbote, B.L.; McGuire, K.; Karimullah, A.S.; Robbie, J.; Sloan, W.T.; et al. A cross-reactive plasmonic sensing array for drinking water assessment. *Environ. Sci. Nano* **2023**, *10*, 3500–3508. [CrossRef]
241. Ahmed, F.; Azim, M.A.; Zubair, A. High sensitivity terahertz metamaterial sensor for trace pesticide detection. *RSC Adv.* **2025**, *15*, 20530–20541. [CrossRef]
242. Vural Kaymaz, S.; Özen, M.; Çelik, S.; Tanrıseven, S.; Olgun, E.E.O.; Canlı, O.; Güzel, B.; Sarıkaya, Y.; Kurt, H.; Yüce, M. Hexagonal Au Nanostructure SERS Metasurface for AI-Driven Detection of Pesticide Residues in Real Food Samples. *ACS Appl. Nano Mater.* **2026**, *9*, 7220–7237. [CrossRef]
243. Amiri, M.; Abolhasan, M.; Shariati, N.; Lipman, J. Soil moisture remote sensing using SIW cavity based metamaterial perfect absorber. *Sci. Rep.* **2021**, *11*, 7153. [CrossRef]
244. Shafi, M.; Duan, P.Y.; Liu, W.Y.; Zhang, W.J.; Zhang, C.; Hu, X.X.; Zha, Z.P.; Liu, R.C.; Liu, C.; Jiang, S.Z.; et al. SERS Sensing Using Graphene-Covered Silver Nanoparticles and Metamaterials for the Detection of Thiram in Soil. *Langmuir* **2022**, *38*, 16183–16193. [CrossRef]
245. Liu, C.; Wang, S.H.; Dong, X.; Huang, Q. Flexible and Transparent SERS Substrates Composed of Au@Ag Nanorod Arrays for In Situ Detection of Pesticide Residues on Fruit and Vegetables. *Chemosensors* **2022**, *10*, 423. [CrossRef]

246. Wang, J.X.; Xie, B.B.; Liu, Y.M.; Cui, M.H.; Zhang, X.; Wang, G.J.; Sun, K.; Cao, Z.C.; Zeng, H.C.; Jin, Q.X.; et al. SoilNutri: A Passive Metasurface-based, Low-cost System for Soil Moisture and Nitrogen Monitoring. *Proc. ACM Interact. Mob. Wearable Ubiquitous Technol.* **2026**, *10*, 19. [CrossRef]
247. Chen, Y.X.; Chen, R.P.; Wang, H.; Pan, D.X.; Zhou, M.T.; Yang, L.; Ma, Z.; Zhang, F.; Zhao, J.W.; Tang, X.F.; et al. Photonic Crystal Microsphere-Based SERS Biosensor for Ultrasensitive Detection of Aflatoxin B1 in Feed. *ACS Omega* **2026**, *11*, 6123–6132. [CrossRef]
248. Veliz, L.; Galarreta, B.C.; Lagugne-Labarthet, F. Flow-Through Aptamer-SERS Microfluidic Platform for Aflatoxin B1 Detection in Food Crops. *ACS Omega* **2026**, *11*, 40905–40915. [CrossRef]
249. Clinical and Laboratory Standards Institute. *Evaluation of Detection Capability for Clinical Laboratory Measurement Procedures*; Approved Guideline—Second Edition; CLSI Document EP17-A2; Clinical and Laboratory Standards Institute: Wayne, PA, USA, 2012.

Disclaimer/Publisher's Note: The statements, opinions and data contained in all publications are solely those of the individual author(s) and contributor(s) and not of MDPI and/or the editor(s). MDPI and/or the editor(s) disclaim responsibility for any injury to people or property resulting from any ideas, methods, instructions or products referred to in the content.